environments

MDPI

Article

Preliminary Radiological Dose Assessment: A Case Study of Tourist Caves in Pacitan, Indonesia

Faza A. An'umillah [1], Johan A. E. Noor [1,*], Yahya Efendi [1], Khoirul Anwar [2], Nurul Annisa [3], Adinda T. Desviana [4,5], Wahyudi [5], Agus N. Rachman [5], Muhammad M. Farid [5], Radhia Pradana [5,6], Shinji Tokonami [6], Chutima Kranrod [6], Oumar B. Modibo [7] and Eka Djatnika Nugraha [5,8,*]

1 Department of Physics, Faculty of Sciences, Technology, and Mathematics, Brawijaya University, Malang 65145, Indonesia; fazaatika24@gmail.com (F.A.A.); yahya_efendi@student.ub.ac.id (Y.E.)
2 Department of Informatics, Faculty of Science and Technology, University of Technology Yogyakarta, Sleman 55285, Indonesia; anwarrudong230@gmail.com
3 Department of Physics, Faculty of Mathematics and Natural Sciences, Bandung Institute of Technology, Bandung 40132, Indonesia; nurula200700@gmail.com
4 Department of Environmental Engineering, Faculty of Civil and Environmental Engineering, Bandung Institute of Technology, Bandung 40132, Indonesia; adin007@brin.go.id
5 Research Center for Safety, Metrology, and Nuclear Quality Technology, Research Organization for Nuclear Energy, National Research and Innovation Agency (BRIN), South Tangerang 15314, Indonesia; wahy008@brin.go.id (W.); agus136@brin.go.id (A.N.R.); muha123@brin.go.id (M.M.F.); h24dh203@hirosaki-u.ac.jp (R.P.)
6 Institute of Radiation Emergency Medicine (IREM), Hirosaki University, Hirosaki 036-8564, Japan; tokonami@hirosaki-u.ac.jp (S.T.); kranrodc@hirosaki-u.ac.jp (C.K.)
7 Research Center for Nuclear Science and Technology, Institute of Geological and Mining Research, Yaoundé P.O. Box 4110, Cameroon; bobbomodibo@gmail.com
8 The Indonesian Embassy/Permanent Mission in Vienna, 1180 Vienna, Austria
* Correspondence: jnoor@ub.ac.id (J.A.E.N.); ekad001@brin.go.id (E.D.N.)

Abstract

Karst caves can accumulate elevated radon concentrations, potentially increasing radiation exposure among visitors and workers. This preliminary study assessed the potential radiological exposure in twelve karst caves in Pacitan, Indonesia. Radon concentrations were measured using passive and active methods, and ambient dose equivalent rates were determined to estimate annual effective doses under different assumed exposure scenarios. Laman Cave exhibited the highest mean active and passive radon concentrations of 71,003 ± 2499 and 29,893 ± 1426 Bq m^{-3}, respectively, and the highest ambient dose equivalent rate of 578 nSv h^{-1}. Estimated public doses remained below the selected public dose screening criterion of 1 mSv $year^{-1}$. Under the worst-case occupational exposure scenario (2080 h $year^{-1}$), the estimated total annual effective doses exceeded the selected screening criterion of 20 mSv $year^{-1}$ in 36 of the 45 evaluated cave segments. Under the moderate occupational exposure scenario (520 h $year^{-1}$), the number of segments exceeding this criterion decreased to ten, located in five segments at Gong, all segments at Laman and one segment at Tabuhan Caves, with a maximum estimated annual effective dose of 233.3 mSv $year^{-1}$. These preliminary findings identify locations with potentially elevated radiation exposure and highlight the importance of targeted monitoring and occupancy management. However, long-term monitoring and site-specific validation are necessary before establishing year-round management recommendations.

Keywords: ambient dose equivalent rate; effective dose; external exposure; inhalation exposure; radon

Check for updates

Academic Editors: Marius M. Cazacu and Brindusa Sluser

Received: 9 October 2026
Revised: 13 November 2026
Accepted: 15 November 2026
Published: 23 November 2026

Copyright: © 2026 by the authors. Licensee MDPI, Basel, Switzerland. This article is an open access article distributed under the terms and conditions of the Creative Commons Attribution (CC BY) license.

1. Introduction

Indonesia has diverse natural landscapes that support ecotourism. One important destination is Pacitan Regency in East Java Province, located within the Gunungsewu karst area, a UNESCO Global Geopark [1,2]. In general, this area features interesting geological phenomena, unique hydrogeology, beautiful scenery, and rich geological heritage that support its geopark status [3]. Pacitan is also known as the "City of 1001 Caves" because of its numerous caves [4]. Among them, Gong Cave is popular for its stalactite and stalagmite formations, while Tabuhan Cave is known for its acoustically resonant speleothems and archeological remains [5,6]. These geological features attract many visitors [7]. According to the Department of Tourism, Culture, Youth, and Sports of Pacitan Regency, Gong and Tabuhan Caves received an average of 147,928 and 10,641 visitors manually, respectively, from 2017 to 2025. High visitor activity can influence environmental conditions within caves, including temperature, relative humidity (RH), airflow, and ventilation [8]. Increased visitor numbers may also contribute to elevate carbon dioxide (CO_2) and particulate matter (PM) concentrations, potentially affecting cave conservation and indoor air quality [9–12]. Understanding these environmental characteristics is therefore important for assessing potential health risks in tourist caves [13].

In addition to CO_2 and PM caves can contain radon (^{222}Rn), a naturally occurring radioactive gas and classified as a Group 1 carcinogen [14]. Radon is produced through the radioactive decay of radium-226 (^{226}Ra) in the uranium (^{238}U) decay series. Once released into cave air, radon decays into short-lived radioactive progeny, which can be inhaled and deposited in the respiratory tract, thereby increasing the risk of lung cancer [15–19]. Radon is globally recognized as the second leading cause of lung cancer after smoking and the leading cause among nonsmokers [20,21]. Radon can accumulate in poorly ventilated and low-lying environments, including karst caves [21,22]. Its concentrations is influenced by cave morphology, airflow, and temperature differences between the cave interior and the outside environment [23,24]. Although tourists are generally exposed for short periods, cave workers such as tour guides and maintenance staff may experience higher cumulative radon exposure due to longer occupancy duration [25,26]. Previous studies in tropical karst caves have reported radon concentrations ranging from 10 to 80,000 $Bq \cdot m^{-3}$, with estimated effective doses ranging from 0.77 to 347 mSv $year^{-1}$ [27–35]. Inhalation of radon, thoron, and their progeny contributes approximately 60% (1.8 mSv) of the total annual effective dose from natural radiation sources (3.0 mSv) [36], highlighting the potential for significant radiation exposure in confined karst caves.

Although previous studies have reported the spatial and temporal variability of radon concentrations and associated inhalation risks in tourist caves, integrated assessments of radon inhalation and ambient dose equivalent rate remain limited, particularly in tropical karst tourist caves. In Indonesia, baseline data combining radon concentrations, ambient dose equivalent rates, and potential annual effective doses for cave workers and visitors are still unavailable. Preliminary assessments are therefore needed to identify potentially elevated radon exposure locations and inform further radiological investigations. Both the United Nations Scientific Committee on the Effects of Atomic Radiation (UNSCEAR) and the International Commission on Radiological Protection (ICRP) provide scientific information and guidance for assessing radiation exposure and potential health risks. The ICRP recommends annual effective dose limits of 20 mSv $year^{-1}$ for occupational exposure and public exposure to 1 mSv $year^{-1}$ [36–39]. These limits are also used by the Indonesian Nuclear Energy Regulatory Agency (BAPETEN) [40]. However, specific dose criteria for natural radon exposure in tourist caves have not been identified in the regulations reviewed. Therefore, this study uses the values of 20 mSv $year^{-1}$ and 1 mSv $year^{-1}$ as preliminary

screening criteria for cave workers and visitors, respectively, rather than as regulatory limits directly applicable to tourist caves.

This preliminary study assessed potential radiation exposure in 12 tourist karst caves in Pacitan, Indonesia by measuring radon concentrations, ambient dose equivalent rates, and environmental parameters. Spatial variations within and among caves were characterized and potential annual effective doses were estimated under assumed visitor and worker occupancy scenarios. Cave entrance characteristics and segment morphology were also documented to provide broad context for interpreting spatial variations in radon concentrations and radiological measurements (Table S2). The findings aim to provide initial baseline data, identify locations requiring further monitoring, and inform provisional radiation protection and cave-management strategies rather than to establish definitive year-round exposure conditions or safe occupancy limits. This study also supports the Sustainable Development Goals (SDGs), particularly SDG 3.9 (reducing environmental health risks), SDG 8.8 (occupational safety), SDG 12.b (monitoring the impacts of sustainable tourism), and SDG 11.4 (protecting cultural and natural heritage).

2. Materials and Methods

2.1. Environmental and Geological Setting of Study Area

Pacitan Regency, East Java Province, is located within the Gunungsewu karst area along the southern coast of Java Island. It is bordered by Ponorogo, Trenggalek, and Wonogiri Regencies to the north and east, and the Indian Ocean to the south [5]. The regional landscape is characterized by rugged, highly karst topography, with approximately 49% of the area having slopes exceeding 40% [4]. Field monitoring was conducted from January to February 2026 during the regional wet monsoon season to characterize cave microclimatic parameters under conditions of high-humidity and limited natural ventilation. Environmental and radiological data collection was conducted across 12 karst caves distributed across the regency (Figure 1). These sites were purposively selected to capture structural and anthropogenic heterogeneity, including differences in tourism status (commercialized vs. non-commercialized), geographic distribution, internal cave morphology, and baseline ventilation characteristics. The spatial coordinates, spatial dimensions, speleothem characteristics, and morphology profile of the 12 cave microenvironments are systematically provided in Tables S1 and S2.

The investigated caves were divided into two clusters. The western cluster includes Gong, Kalak, Tabuhan, Putri, Dawung, Semedi, Kendil, and Selo Arum Caves, which are located within a relatively heterogeneous geological setting composed mainly of Wonosari, Oyo, Nampol, Wuni, and Jaten Formations. Several mapped structural features also across or occur near this cluster, including the Rohtawu, Grendulu, Buyutan, Punung, and Pucuklangan Faults. Meanwhile, the eastern cluster consists of Somopuro, Jurug Jaran, Laman, and X Caves, which are more closely grouped and predominantly located within the Jaten Formation. Several nearby intrusive bodies mapped as Tomi (ba) occur around of it, while the Kayuwayang Fault crosses the area in a northeast–southwest direction. Somopuro and Jurug Jaran Caves are located closer to the northern part of the Jaten Formation, whereas Laman and X Caves occur farther south, close to lithological contacts and nearby intrusive bodies [41,42]. The geological units and numbered Tomi intrusive bodies shown in Figure 1 are further described in Table 1. These regional geological settings were used as the basis for the subsequent GIS analysis of cave proximity to mapped faults, intrusive bodies, and lithological contacts.

Table 1. Geological units and relative ages in the study area, arranged from oldest to youngest.

Map Code	Geological Unit	Lithology	Geological Age
Toma	Arjosari Formation	Polymit conglomerate, sandstone, siltstone, limestone, claystone, sandi marl, pumiceous sandstone, intercalated by volcanic breccia, lava, and stuff.	Late Oligocene–Early Miocene
Tomm	Mandalika Formation	Interbedded of volcanic breccia, lava, tuff; intercalated by tuffaceous sandstone, siltstone, and claystone.	
Tomi	Intrusive Rocks (1)	(an) andesite	Oligocene–Miocene
	Intrusive Rocks (2,3)	(da) dasit	
	Intrusive Rocks (4,5,6)	(ba) basal	
Tmj	Jaten Formation	Conglomerate, conglomeratic sandstone, tuffaceous sandstone, mudstone, lignite, carbonaceous shale, tuff; sulphuric in places.	Middle Miocene
Tmw	Wuni Formation	Volcanic breccia, tuff, tuffaceous sandstone, lithic sandstone, and siltstone, with intercallations of lignite and limestone, locally containing blocks of silificied wood.	
Tmn	Nampol Formation	Tuffaceous sandstone, siltstone, tuffaceous limestone, claystone, and lignite with intercallations of conglomerate and breccia	
Tmo	Oyo Formation	Calcaerous sandstone, tuffaceous sandstone, calcareous siltstone, tuffaceous limestone, sandy mart, and tuffaceous mart.	Middle–Late Miocene
Tmwl	Wonosari Formation	Reef limestone, bedded limestone, fragmental limestone, sandy limestone, and marl.	
Qa	Alluvium	Cobble, pebble, sand, silt, clay, and mud.	Holocene–Recent

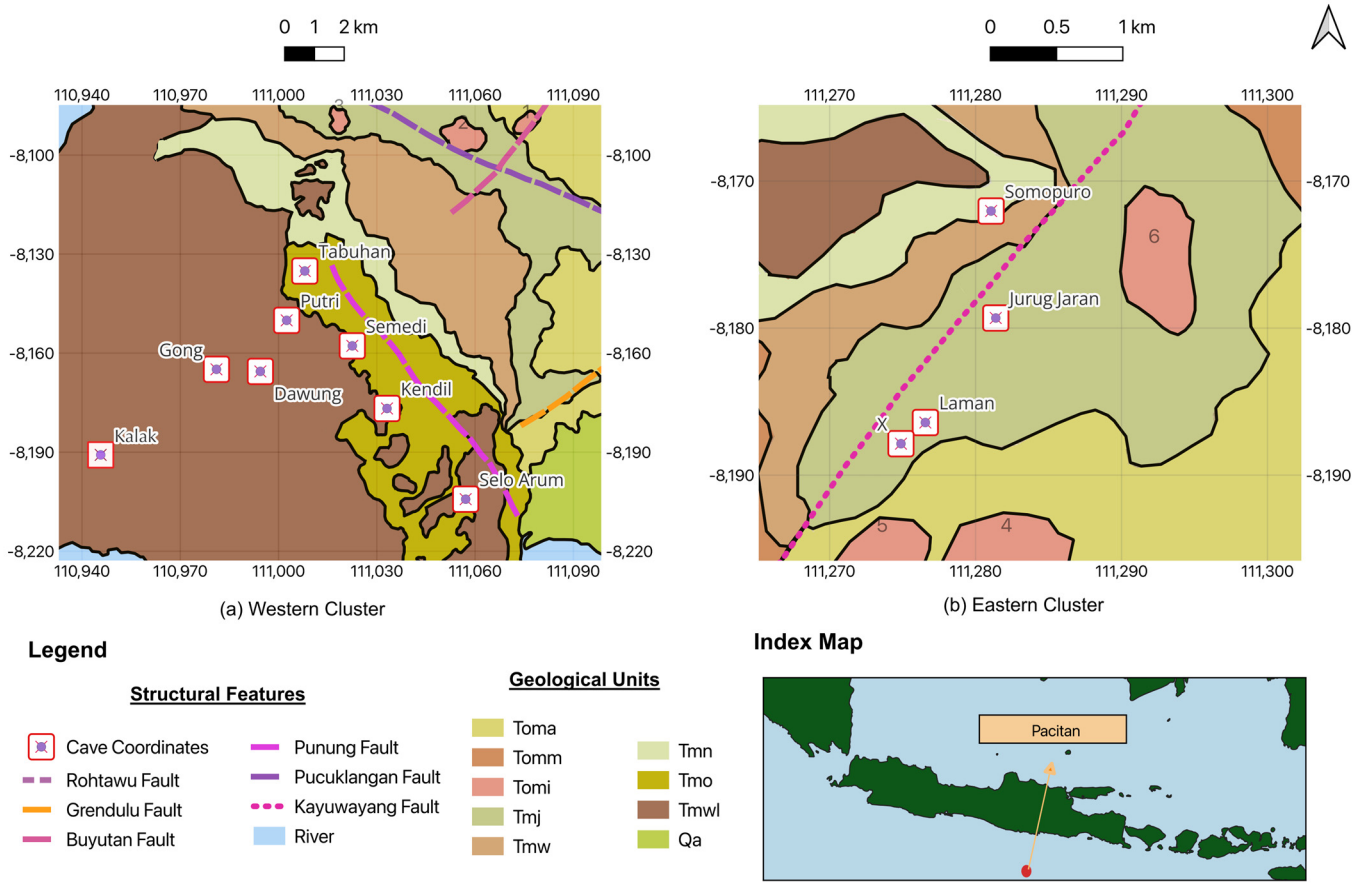

Figure 1. Geographic distribution of selected cave sampling sites in Pacitan, Regency, East Java, Indonesia: (**a**) Western Cluster (**b**) Eastern Cluster. The index map indicates the location of study area (adapted from [41,43,44]). The study-area map was prepared using QGIS version 3.44.15 "Solothurn" is licensed under the GNU General Public License (GPL) version 2.

2.2. RADUET Preparation and Calibration

To ensure the accuracy of long-term cumulative radon and thoron exposure measurements, passive RADUET (Radosys Ltd., Budapest, Hungary) detectors were calibrated at the Environmental Radiation Laboratory, Institute of Radiation Emergency Medicine (IREM), Hirosaki University, Japan. The calibration facility consisted of a radon/thoron source unit, a mixing chamber, an exposure chamber, and a reference monitoring unit [45]. Natural uranium-bearing rock samples were used as the ^{222}Rn source, while gas-lantern mantles were used as the ^{220}Rn source.

The generated radon gas was transferred into the exposure chamber using an automated air pump system. Calibrations for ^{222}Rn and ^{220}Rn were conducted separately. Because of the short half-life of ^{220}Rn ($T_{1/2}$: 55.6 s), the mixing chamber was also used as the direct thoron exposure chamber. ^{222}Rn and ^{220}Rn concentrations were maintained at a steady-state ranges of 200–1000 Bq m^{-3} and 3500–30,000 Bq m^{-3}, respectively. The passive detectors were exposed separately at three time-integrated exposure levels (low, medium, and high) for each gas. Reference concentrations were continuously monitored using calibrated reference instruments, specifically an ALPHAGUARD ionization chamber for ^{222}Rn, and synchronized Pylon AB-5 and RAD7 for ^{220}Rn. Temperature, RH, and air pressure inside the calibration chamber were continuously monitored to ensure the stable experimental conditions [46–48].

Before field deployment, RADUET detectors were stored in airtight plastic packaging and sealed using a vacuum-sealing machine to prevent premature radon infiltration and background track accumulation. Solid-state track detectors (CR-39) were individually inserted into the paired diffusion chambers as illustrated in Figure 2. The RADUET discrimination mechanism of radon and thoron is based on differences in air-exchange rates between its two diffusion chambers. The low air-exchange rate chamber records radon because gas diffuses slowly through a narrow gap between the lid and the bottom of the chamber. The high air-exchange rate chamber is equipped with six holes covered by electro-conductive sponges that filter out aerosols and decay products, allowing both radon and thoron to enter. The paired chambers were assembled into a single monitoring unit using cable ties and kept vacuum-sealed until deployment at the measurement site [48].

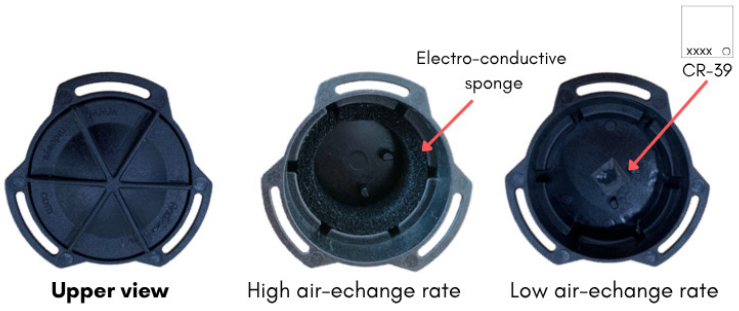

Figure 2. Schematic upper view of RADUET.

2.3. Field Measurement and Data Collection

During field sampling, monitoring locations, sampling dates and times, and GPS coordinates were systematically recorded.

2.3.1. Ambient Dose Equivalent Rate ($H^*(10)$) Measurement

Ambient dose equivalent rate ($H^*(10)$, μSv h^{-1}) were executed at a standardized height of 1.0 m above the ground to represent the typical human whole-body exposure height [49]. Measurement locations were selected to characterize spatial radiation heterogeneity, including cave entrances, locations 1–10 m from entrances, and near RADUET

detectors deployment. At each location, $H^*(10)$ values were recorded three times at 1 min intervals to guarantee stable data. The representative caves (Gong, Tabuhan, and Laman Caves) were monitored for three consecutive days (nine measurements per location) to observe short-term temporal variations. The rest of the caves were measured on a single day (three measurements per location) to provide baseline spatial comparison. Measurements for each cave segment were averaged to get a representative mean $H^*(10)$ values. $H^*(10)$ measurements were performed using a Pegasus Pro portable high sensitivity CsI(Tl) scintillation gamma survey meter with μSv h^{-1} unit (Fuji Electric Co., Ltd., Tokyo, Japan). The measured $H^*(10)$ is recorded with μSv h^{-1} then convert to nSv h^{-1}.

2.3.2. Microclimate Parameter Monitoring

Microclimate parameters were monitored by continuously recording CO_2 (ppm), RH (%), temperature (°C) and air pressure (hPa) fluctuations. CO_2 concentration was measured using a TR-76Ui non-dispersive infrared (NDIR) CO_2 recorder (T&D Co., Matsumoto, Japan) while temperature, RH, and air pressure were recorded using a TR-73U thermorecorder (T&D Co., Matsumoto, Japan). These parameters were recorded simultaneously with active radon measurements over continuous 3-day monitoring periods at 30 min intervals. This monitoring was conducted in Gong, Tabuhan, and Laman Caves to characterize temporal environmental fluctuations associated with radon.

2.3.3. Airborne PM Measurement

Indoor PM concentrations and size distributions were measured using a handheld TC-8200 6-channel laser particle counter (Dongguan Deyi Electronic Technology Co., Ltd., Dongguan, China). The instrument operates based on light scattering at a sampling flow rate of 1.0 L/min and measures suspended particles in six aerodynamic diameter channels: 0.3, 0.5, 1.0, 2.5, 5.0, and 10 μm. Ambient temperature (range: −10 to 60 °C, accuracy: ± 2 °C) and RH (range: 0 to 100%, accuracy: ± 3%) were recorded simultaneously. Gong Cave was selected as a representative tourist-dense microenvironment. Sequential measurements were conducted at eight designated indoor segments from the cave entrance through Room 7. At each location, triplicate 1 min intervals measurements were conducted before moving to the next segment.

2.3.4. Active In Situ ^{222}Rn Monitoring

Active real-time^{222}Rn measurements were performed in the core chambers of Gong, Tabuhan and Laman Caves using continuous radon monitors selected according to the expected concentration level. In Tabuhan Cave, temporal monitoring was performed using an RD201 RadonEye Alpha (FTLab Co., Ansan, Republic of Korea), which operates based on the pulsed ionization chamber principle, and has a sensitivity of 0.0135 cpm per Bq m^{-3}, with a measurement range of 7.4 to 3699 Bq·m^{-3} [50]. To prevent potential localized microclimatic air current anomalies, the instrument was positioned centrally at a height of 1.0 m above ground. Real-time monitoring in Gong and Laman Caves was performed using an AlphaE Ultra-Small Radon Monitor (Bertin Technologies, Montigny-Ie-Bretonneux, France), which has a measurement range of 20–10,000,000 Bq·m^{-3} [51]. The instrument was positioned at a standardized minimum height 25 cm above the ground. Continuous measurements were conducted for three days in Gong and Tabuhan Caves and one day in Laman Cave.

2.3.5. Passive RADUET Measurement

At each selected monitoring point, the vacuum-sealed packaging was unsealed, and initial exposure time (T_{start}) was recorded. The paired RADUET assemblies were deployed at a height of 1.0–2.0 m above ground. The passive RADUET measurements were conducted for approximately one month to obtain integrated concentration estimation over the monitoring period. Upon retrieval, the final exposure time (T_{end}) was recorded, and

retrieved CR-39 were instantly resealed in airtight bags to prevent the detectors from further environmental exposure during transportation to the laboratory. The details about RADUET deployment are provided in Table S3.

2.3.6. CR-39 Etching and Analysis

Following field retrieval, CR-39 detectors exposed to ^{222}Rn and ^{220}Rn were chemically etched using a 6 M NaOH solution at 60 °C for 24 h, following the standard protocol provided by Nagase Landauer, Ltd. (Ibaraki, Japan) [48]. This etching enlarges the latent submicroscopic molecular damage tracks produced by alpha-particle interactions into visible tracks suitable for quantification [52]. The etching process was done at the Research Center for Safety, Metrology, and Nuclear Quality Technology, Research Organization for Nuclear Energy, National Research and Innovation Agency, Indonesia.

The etched CR-39 detectors were transferred to the Institute of Radiation Emergency Medicine, Hirosaki University, Japan for track density analysis. Microscopic analyses were performed using a Nikon Eclipse Ci optical microscope system (Nikon Corporation Healthcare Business Unit, Yokohama, Japan) configured at a total magnification of 100 times (via 10× eyepiece and 10 objective lens). Microscopic observations were systematically conducted across 10 designated fields of view per detector to ensure representative surface quantification. Images were captured using a high-resolution Nikon D5200 digital camera system attached to the microscope port, recording track densities at a spatial resolution of 6000 × 4000 pixels per field of view. Then the calculation of the recorded track density was performed using ImageJ (version 1.54g) programming.

Integrated ^{222}Rn and ^{220}Rn concentrations were calculated by substituting the net track densities into Equations (1) and (2) [53]. In these equations, $\overline{C_{Rn}}$ and $\overline{C_{Tn}}$ represent the time-averaged radon and thoron concentrations (Bq·m^{-3}) during the exposure period; d_L and d_H indicate the total measured alpha track densities (track·m^{-2}) obtained from the low and high air-exchange rate chambers of the RADUET deployment, respectively. The terms of f_{Rn1} and f_{Tn1} represent the ^{222}Rn and ^{220}Rn calibration coefficients for the low air-exchange rate chamber, whereas f_{Rn2} and f_{Tn2} represent the corresponding coefficients for the high air-exchange rate chamber (track·m^{-2}·kBq·m^{3}h^{-1}). Lastly, t is the total field exposure duration in hours, and $\overline{b}$ is the baseline background track density (track·m^{-2}) derived from unexposed CR-39 control detectors.

$$\overline{C}_{Rn} = \left(d_L - \overline{b}\right) \times \frac{f_{Tn2}}{t \times (f_{Rn1} \times f_{Tn2} - f_{Rn2} \times f_{Tn1})} - \left(d_H - \overline{b}\right) \times \frac{f_{Tn1}}{t \times (f_{Rn1} \times f_{Tn2} - f_{Rn2} \times f_{Tn1})} \quad (1)$$

$$\overline{C}_{Tn} = \left(d_H - \overline{b}\right) \times \frac{f_{Rn1}}{t \times (f_{Rn1} \times f_{Tn2} - f_{Rn2} \times f_{Tn1})} - \left(d_L - \overline{b}\right) \times \frac{f_{Rn2}}{t \times (f_{Rn1} \times f_{Tn2} - f_{Rn2} \times f_{Tn1})} \quad (2)$$

Uncertainties of^{222}Rn and ^{220}Rn concentrations were calculated using Equations (3)–(6), respectively [18,48].

$$W_1 = \frac{f_{Tn2}}{t \times (f_{Rn1} \times f_{Tn2} - f_{Rn2} \times f_{Tn1})}; W_2 = \frac{f_{Tn1}}{t \times (f_{Rn1} \times f_{Tn2} - f_{Rn2} \times f_{Tn1})} \quad (3)$$

$$W_3 = \frac{f_{Rn1}}{t \times (f_{Rn1} \times f_{Tn2} - f_{Rn2} \times f_{Tn1})}; W_4 = \frac{f_{Rn2}}{t \times (f_{Rn1} \times f_{Tn2} - f_{Rn2} \times f_{Tn1})} \quad (4)$$

$$u_{Rn} = k \cdot \sqrt{{W_1}^2({u_{dL}}^2 + {u_b}^2) - 2W_1W_2{u_b}^2 + {W_2}^2({u_{dH}}^2 + {u_b}^2) + \frac{({d_H}^2 - 2\,\overline{b} \cdot d_H + \overline{b}^2){W_2}^2 + {\overline{C}_{Rn}}\left(2d_H - \overline{2b}\right)W_2 + {\overline{C}_{Rn}}^2}{{W_1}^2}{u_{w1}}^2 + (-d_H + \overline{b})^2{u_{w2}}^2} \quad (5)$$

$$u_{Tn} = k \cdot \sqrt{W_3{}^2(u_{dH}{}^2 + u_b{}^2) - 2W_3W_4u_b{}^2 + W_4{}^2(u_{dL}{}^2 + u_b{}^2) + \frac{(d_L{}^2 - 2\,\overline{b} \cdot d_L + \overline{b}^2)W_4{}^2 + \overline{C}_{Tn}\left(2d_L - \overline{2b}\right)W_4 + \overline{C}_{Tn}{}^2}{W_1{}^2} u_{w3}{}^2 + (-d_L + \overline{b})^2 u_{w4}{}^2} \quad (6)$$

where u_{dL} and u_{dH} are the standard uncertainty from the alpha track densities in low and high air-exchange rate chambers, respectively; u_b is the standard uncertainty of background density, respectively; u_{W1} and u_{W2} are the combined standard uncertainty of radon coefficient in low and high air-exchange rate chambers, respectively; u_{W3} and u_{W4} are the combined standard uncertainty of thoron coefficient in low and high air-exchange rate chambers, respectively; and k is a coverage factor of 1.96 for a 95% confidence interval.

2.4. Radiological Dose Assessment

2.4.1. Internal Effective Dose (E_{in})

The World Health Organization (WHO) recommends a reference level of 100 Bq m^{-3} for indoor environments, with a maximum reference level of 300 Bq m^{-3} under specific local conditions [54]. The ICRP and International Atomic Energy Agency (IAEA) also recommended 300 Bq m^{-3} as an upper reference level for occupational exposure in workplaces and managed tourist caves [55,56]. The annual internal effective dose (E_{in}, mSv year^{-1}) from radon inhalation was estimated using the radon concentration obtained from Equation (1) and used for Equation (7) [36,39].

$$E_{in} = C_{Rn} \times DCF \times t_{occ} \times \frac{F_{eq}}{0.4} \quad (7)$$

where F_{eq} is the radon progeny equilibrium factor and DCF is the dose conversion factor. A constant value of F_{eq} = 0.4 was used based on reference values for radon exposure assessment in cave environments [36,39]. Following ICRP Publication 137, a DCF of 1.5×10^{-5} mSv (Bq h m^{-3})$^{-1}$ was applied to both cave workers and visitors. This coefficient corresponds to ICRP recommendation to the recommended value of 24 mSv/WLM for radon exposure in tourist caves, using a reference F_{eq} and the conversion relationship of 1 WLM = 6.37×10^{-5} mSv (Bq h m^{-3})$^{-1}$/F_{eq} [38]. The same DCF was applied to both groups because their exposure scenarios concerned the same type of environment that is tourist caves. Differences between the scenarios were represented by their respective assumed annual exposure durations (t_{occ}, h year^{-1}) (Table 2).

Table 2. Annual occupancy (t_{occ}) baselines and exposure profiles for various occupational categories and visitors in caves based on UNSCEAR guidelines.

Exposure Scenario	t_{occ} (h/Year)	Occupational Category	Justification
Worst case	2080	Tour guides and local photographers	The worst-case scenario did not represent realistic occupancy time but represent the highest possible occupancy time under legal working limit per year (40 h per weeks, 52 weeks per year) based on Labor laws No. 13 [49,57].
Moderate case	520	Maintenance staff and cave flashlight providers	Moderate-case scenario gives closer representation for the tour guide occupancy time. It should be noted that the actual duration of each trip and total trip per week would have wide variation depending on each visitor and visitor availability. In this study, assumption of 10 trips per week with one hour duration per trip was used [58].
Public	1	Visitors	Public scenario represents a literature-based assumption rather than a measured visit duration [58]. For visitors who enter the caves multiple times per year, the annual exposure duration should be adjusted according to the actual duration per visit and total number of visits per year.

2.4.2. External Effective Dose (E_{ex})

The UNSCEAR recommends $H^*(10)$ as an operational quantity for estimating effective dose [36]. It is used to assess penetrating external radiation fields and their potential contribution to human exposure [59]. The annual effective dose (E_{ex}, mSv year^{-1}) was calculated by combining the measured $H^*(10)$ values with the corresponding annual occupancy times using Equation (8).

$$E_{ex} = H*(10) \times CF \times 10^{-6} \times t_{occ} \quad (8)$$

where CF is the conversion coefficient from $H^*(10)$ to E_{ex}, and 10^{-6} is the unit conversion factor that converts nano (nSv) to milli (mSv) unit. Following the radiological protection approach adopted by [60], a dimensionless conversion factor (CF) of 0.6 was applied to convert $H^*(10)$ in external effective dose for both public and occupational exposure scenarios.

2.4.3. Annual Effective Dose (E_{total})

The total annual effective dose was calculated as the sum of the internal and external effective doses [36]:

$$E_{total} = E_{in} + E_{ex} \quad (9)$$

The calculated E_{total} values were compared with annual dose criteria of 20 mSv year^{-1} for occupational exposure and 1 mSv year^{-1} for public exposure, which were used as preliminary screening benchmarks in this study [36,38,39]. The calculation framework for both exposure pathways is presented in Figure S1.

2.4.4. Estimation of Provisional Maximum Allowable Annual Occupancy Time (t_{max})

The provisional maximum allowable annual occupancy time (t_{max}) for each cave segment was calculated from the E_{total}. The t_{max} value was estimated using Equation (10). To further assess the maximum occupancy duration under a specified dose limit, t_{max} was derived from the total effective dose rate. The derivation and mathematical relationship between t_{max} and the assumed occupancy time are provided in Appendix A.

$$t_{max} = \frac{E_{ref} \cdot t_{occ}}{E_{total}} \quad (10)$$

where $\dot{E}(t)$ is the time-dependent effective dose rate (mSv h^{-1}), $\dot{E}_{total}$ is the total effective dose rate (mSv h^{-1}), $\dot{E}_{in}$ is the internal effective dose rate from radon inhalation (mSv h^{-1}), $\dot{E}_{ex}$ is the external effective dose rate from gamma radiation (mSv h^{-1}), and E_{ref} is the selected screening reference dose (mSv year^{-1}).

2.4.5. Proposed Preliminary Zoning and Cave Radiation Management

To support preliminary radiation management zones, the measured radon concentrations and the estimated effective doses were interpreted using a proposed site-specific zoning framework comprising normal-access, controlled-access, and restricted-access zones. The framework adopts a graded approach based on the recommendations of the ICRP and the IAEA, whereby protective measures are adjusted according to the level of exposure [55,61]. Normal-access zones are characterized by comparatively low radon concentrations and estimated doses below the selected management reference level, supporting regular monitoring with periodic monitoring. Controlled-access zones include areas where radon concentrations are higher, or workers spending a long time within the cave may increase their E_{total}. These categories are proposed operational measures for investigated caves rather than universally prescribed regulatory classifications. In these areas, limited time access, work rotations, and radon monitoring are suggested to be done more frequently (semi-annual to quarterly) [26,62]. Restricted-access zones are proposed for areas where

high radon concentrations and estimated occupational doses indicate that exposure could approach or exceed the selected dose criteria under moderate or worst-case occupancy assumptions [14,62]. The resulting categories are provisional and depend on the occupancy assumptions and dose-estimation method used.

Segments with estimated doses below 10 mSv·y^{-1} were assigned to the normal-access category; doses from 10 to 20 mSv year^{-1} were categorized as controlled-access, and segments with doses exceeding 20 mSv year^{-1} were assigned to the restricted-access category. The 10 mSv year^{-1} value was selected with reference to the benchmark discussed in ICRP Publication 126, whereas 20 mSv year^{-1} was considered in the context of the occupational dose limit recommended [55]. ICRP Publication 126 also recommends an upper derived reference level of 300 Bq·m^{-3} and encourages national authorities to establish reference levels within the range of 100– 300 Bq m^{-3}. Accordingly, concentrations below 100 Bq·m^{-3} were classified as low, 100–300 Bq m^{-3} as elevated, and above 300 Bq m^{-3} as high for preliminary zoning. These proposed thresholds were adopted as study-specific management criteria and do not represent formal ICRP zoning threshold or Indonesian regulatory classifications for caves. The assigned categories in Table 3 were intended to support preliminary decisions on monitoring, occupancy control, and access review, and should be reassessed as additional measurements and representative occupancy data become available.

Table 3. Proposed preliminary access-zone classification criteria for cave workers based on radon concentration and estimated annual effective dose.

Assessment Parameter	Indicator	Normal-Access Zone	Controlled-Access Zone	Restricted-Access Zone
C_{Rn} (Bq·m^{-3})	Screening	<100	$100 < C_{Rn} \leq 300$	>300
E_{total} (mSv·y^{-1})	Radiological Risk	<10	$10 < E_{total} \leq 20$	>20

These categories represent proposed management thresholds, not regulatory limits, or declarations of safe exposure.

2.5. Statistical Analysis

Statistical analyses and data visualization were performed using Python (version 3.15.2) and OriginPro 2026b (OriginLab Corporation, Northampton, MA, USA). Python was used in a local Windows environment, while additional analyses were conducted using Python (version 3.x) in Google Collaboratory. The NumPy and SciPy libraries were used for numerical computations and statistical testing, where applicable. The Shapiro–Wilk test was first applied to check the normality of PM concentrations, RH, temperature, and radon concentration from passive monitors. Spearman's rank correlation with a two-tailed test was used to assess monotonic relationships between variables.

For the airborne PM analysis in Gong Cave, Spearman's rank correlation was used to evaluate the relationships among the different PM size fractions and between PM concentrations and the environmental parameters (RH and temperature). For the spatial analysis of passive radon concentration, Spearman's Rank correlation of permutation test was used to assess the monotonic relationship between radon concentration and distance from cave entrance. For $H^*(10)$, the Kruskal–Wallis test was used to assess whether significant spatial variation existed among the measured cave segments. When a significant overall difference was identified, Dunn's post hoc test was performed for pairwise comparisons between specific segments and adjusted using Bonferroni method. A $p\text{-}value < 0.05$ was considered statistically significant for all statistical tests.

2.6. Spatial Analysis

Spatial analysis was conducted using QGIS to examine the spatial relationships between the investigated caves, mapped faults, and geological units in the study area. Cave

coordinates obtained from field measurements were combined with geological data from the Geological Map of the Pacitan Quadrangle by Samodra et al. (1992) [41,43]. The spatial layers were reprojected to the WGS 84/UTM (Universal Transverse Mercator) Zone 49S coordinate reference system (EPSG:32749) to allow distance measurements in meters. The distances from each cave to the nearest mapped fault, lithological contact, and intrusive body were calculated using the nearest-feature analysis tool in QGIS. The host geological unit of each cave was identified based on the location of its coordinates relative to the mapped geological units. These measurements represent spatial analysis and do not establish a causal relationship between geological features and radon concentrations.

3. Results

3.1. Geological Setting and Spatial Characteristics of the Investigated Caves

3.1.1. Western Cluster

The Punung Fault was identified as the nearest mapped fault for the western cluster (Table 4). The distance to this fault ranged from approximately 986 m at Tabuhan Cave, 1003 m at Semedi Cave to 9911 m at Kalak Cave. Kendil and Selo Arum Caves were also relatively close to the Punung Fault, at approximately 1398 and 1326 m respectively, whereas Gong and Dawung Caves were located farther away, at approximately 5098 and 3914 m. The western caves were mainly located within the Wonosari and Oyo Formations. The distance analysis also identified Wuni Formation as another lithological contact near this area. Semedi Cave showed the shortest distance to the nearest lithological contact, approximately 112 m from the Wonosari Formation, followed by Kendil Cave at 146 m. Putri and Tabuhan Caves were located approximately 604 and 645 m from the nearest contact, respectively. In contrast, Gong, Dawung, and Kalak Caves were located farther from the nearest lithological boundary.

Table 4. Geological setting of the western cluster with mapped faults, intrusive bodies, and lithological contacts.

Cave	Host Geological Unit	Nearest Fault	Distance to Fault (m)	Nearest Lithological Contact	Distance to Contact (m)
Gong	Wonosari Formation	Punung Fault	5098	Oyo Formation Wuni Formation	3355 4857
Tabuhan	Oyo Formation	Punung Fault	986	Wonosari Formation Wuni Formation	645 837
Semedi	Oyo Formation	Punung Fault	1003	Wonosari Formation Wuni Formation	112 1640
Putri	Wonosari Formation	Punung Fault	2237	Oyo Formation Wuni Formation	604 2514
Kalak	Wonosari Formation	Punung Fault	9911	Oyo Formation	7935
Dawung	Wonosari Formation	Punung Fault	3914	Oyo Formation Wuni Formation	2414 4388
Kendil	Wonosari Formation	Punung Fault	1398	Oyo Formation Wuni Formation	146 2628
Selo Arum	Oyo Formation & Wonosari Formation	Punung Fault	1326	Wonosari Formation Wuni Formation	1326 3133

3.1.2. Eastern Cluster

As shown in Table 5, Jurug Jaran Cave was located closest to the Kayuwayang fault at approximately 196 m, followed by X Cave (232 m), Laman Cave (288 m), and Somopuro Cave (344 m). X Cave was the closest site to Tomi (ba)—Intrusion 4, at approximately 580 m, followed by Laman Cave located 747 m. Somopuro Cave and Jurug Jaran Cave were 1010.07 m and 966.03 m away to Tomi (ba)—Intrusion 6, respectively. A similar spatial pattern was observed for lithological contacts. X Cave was located closest to Tmj (140.99 m), followed by Laman Cave, Somopuro Cave, then Jurug Jaran Cave.

Table 5. Geological setting of the eastern cluster with mapped faults, intrusive bodies, and lithological contacts.

Cave	Host Geological Unit	Nearest Fault	Distance to Fault (m)	Nearest Lithological Contact	Distance to Contact (m)
Somopuro	Nampol Formation	Kayuwayang Fault	344	Wuni Formation Wonosari Formation Jaten Formation Tomi (6)	77 213 290 1010
Jurug Jaran	Jaten Formation	Kayuwayang Fault	196	Wuni Formation Arjosari Formation Tomi (6)	725 919 966
Laman	Jaten Formation	Kayuwayang Fault	288	Arjosari Formation Wuni Formation Tomi (4)	210 1129 747
X	Jaten Formation	Kayuwayang Fault	232	Arjosari Formation Wuni Formation Tomi (4)	139 969 580

3.2. Temporal Variation of Radon and Environmental Parameters in Selected Caves

Temporal variations in radon concentration and environmental parameters were investigated in Laman Cave, Gong Cave, and Tabuhan Cave (Figure 3 and Table 6). Laman Cave had extremely high radon concentrations of 60,000–74,000 Bq m^{-3}, indicating a poorly ventilated environment with limited external air circulation. Gong Cave showed concentrations of 7000–9000 Bq m^{-3}, whereas Tabuhan Cave showed lower fluctuations of 1000 to 2200 Bq m^{-3}, suggesting more active air exchange. In Gong and Tabuhan Caves, air pressure showed sinusoidal fluctuations consistent with diurnal cycle. Radon concentrations in Gong Cave increased rapidly before remaining relatively stable at high concentrations, whereas radon in Tabuhan peaked simultaneously with CO_2. Around the 42nd hour, the temperature in Tabuhan Cave increased from 25.2 °C to 25.6 °C, followed by the radon and CO_2 concentrations. This coincided with a significant positive correlation of Spearman test between radon and CO_2 (ρ = 0.357, $p < 0.001$). In contrast, the CO_2 concentrations in Gong and Laman Caves remained above the instrument's upper detection limit of 9999 ppm throughout monitoring, indicating that their actual concentrations exceeded the measurable range.

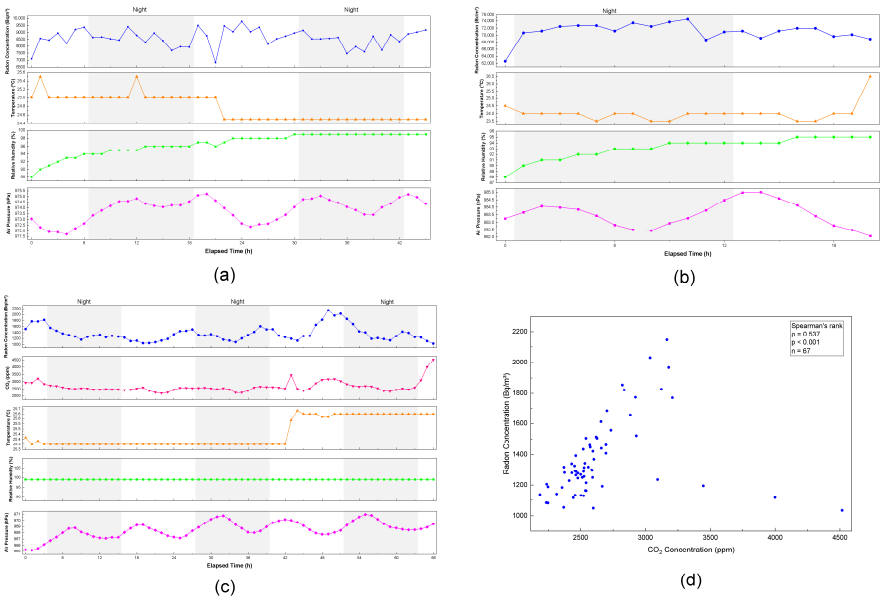

Figure 3. Continuous environmental monitoring and radon correlation analysis across three studied caves: (**a**) Gong Cave, (**b**) Laman Cave, (**c**) Tabuhan Cave, (**d**) Spearman's rank correlation scatter plot between radon and CO_2 in Tabuhan Cave. The shaded region in the figure represents nighttime.

Table 6. Mean radon concentration and environmental parameters measured over time in the studied caves.

Cave	*n*	Radon (Bq m^{-3})	CO_2 (ppm)	Temperature (°C)	RH (%)	Air Pressure (hPa)
Gong	45	8475 ± 1011	>9999 *	25 ± 0.4	96 ± 3.5	974 ± 1.0
Tabuhan	67	1366 ± 249	2652 ± 383	25 ± 0.1	99 ± 0.0	969 ± 1.3
Laman	21	71,003 ± 2499	>9999 *	24 ± 0.6	93 ± 0.8	984 ± 0.8

* CO_2 concentrations exceeded the upper measurement limit (9999 ppm). Values are presented as mean ± standard deviation.

3.3. Spatial Distribution and Size Fractionation of Airborne Particulate Matter in Gong Cave

The PM concentration in Gong Cave exhibited pronounced spatial variability, with mean concentrations ranging from 0.33 to 94,232 μg·m^{-3} and raw measurements from 1.00 and 95,241 μg·m^{-3}. Overall, 98.5% of the measured particles were within the fine fraction (0.3–0.5 μg). Concentrations generally decreased from the entrance toward the inner segments and stabilized in Room 7. $PM_{0.3}$ and $PM_{0.5}$ decreased more sharply than the larger fractions (Figure S2 and Table S4). The Shapiro–Wilk test indicates that only temperature was normally distributed, whereas the other variables deviated from normality (Table S5). Spearman analysis showed positive correlations among PM fractions, ranging from moderate to very strong (ρ = 0.57–0.94, n = 24, p = 0.00001–0.0033). PM fractions also showed significant negative correlations with RH, with strongest relationship observed for $PM_{0.3}$ (ρ = −0.65, n = 24, p = 0.00057), whereas no statistically significant correlations were found between temperature and any PM fractions (ρ = 0.03–0.36, n = 24, p = 0.08696–0.88240).

3.4. Dose Assessments from Inhalation Dose and Ambient Equivalent Dose Rate

3.4.1. ^{222}Rn Concentration and Internal Effective Dose (E_{in})

From 51 RADUET detectors installed across 12 caves in January–February 2026, 45 detectors were successfully retrieved (Table 7). Passive ^{222}Rn concentration ranged from 124 ± 76 Bq m^{-3} at Entrance 2 of Semedi Cave to 29,893 ± 1426 Bq m^{-3} at Point 3 of Laman Cave. Point 4 of Laman Cave showed a similarly high concentration of 29,549 ± 1405 Bq m^{-3}. Except for the entrance of Tabuhan, Kalak and segments of Semedi Caves, concentrations exceeded the 300 Bq·m^{-3} reference level recommended by WHO, ICRP and IAEA. In Gong Cave, ^{222}Rn increased from 1508 ± 202 Bq m^{-3} at the Entrance to 6603 ± 1182 Bq m^{-3} at Room 3, while Tabuhan Cave increased from 286 ± 221 Bq m^{-3} at the Entrance to 2710 ± 404 Bq m^{-3} in the Meditation Room. Most ^{220}Rn measurements were below the Lower Limit of Detection (<LLD). Detectable ^{220}Rn was recorded at Room 4 of Gong Cave, the Entrance of Kalak Cave, Room 1A at Kendil Cave, Room 2 at Somopuro Cave, Point 1 at Laman Cave, Meditation Room of Selo Arum Cave, and Point 2 at X Cave.

Somopuro and Jurug Jaran Caves were excluded from the Shapiro–Wilk test because only one passive radon measurement was available for each cave (Table S7). Spearman's rank correlation analysis showed positive associations between distance from the cave entrance and radon concentration in Gong (ρ = 0.43), Tabuhan (ρ = 0.90), Putri (ρ = 0.40), Kalak (ρ = 0.50), Dawung (ρ = 1.00), Laman (ρ = 0.80), and Selo Arum (ρ = 0.20), whereas negative associations were observed in Semedi (ρ = −0.70) and Kendil (ρ = −0.60) (Table S7). However, none of these observed correlations was statistically significant based on the two-sided permutation tests (p > 0.05). The strength of statistical inference was limited by the small number of observations, particularly in caves with three to five measurements. For Gong Cave (n = 8), the sample size was also limited, and potential dependence among measurement points should be considered when interpreting the correlation result.

Table 7. Concentrations of ^{222}Rn and ^{220}Rn and calculated E_{in} for different occupational categories and visitors in the studied cave.

Cave	Segment	Distance (m) *	Radon Concentration (Bq m^{-3})	Thoron Concentration (Bq m^{-3})	E_{in} (mSv Year^{-1}) Worst Case	Moderate Case	Public
Gong	Entrance	0	1508 ± 202	<LLD	47.1	11.8	0.023
	Room 1	10	1710 ± 276	<LLD	53.3	13.3	0.026
	Room 2	30	4948 ± 762	<LLD	154.4	38.6	0.074
	Room 3	40	6603 ± 1182	<LLD	206.0	51.5	0.099
	Room 4	60	2268 ± 395	6604 ± 1717	70.8	17.7	0.034
	Room 5	100	5718 ± 1013	<LLD	178.4	44.6	0.086
	Room 6	150	3345 ± 897	<LLD	104.4	26.1	0.050
	Room 7	180	3514 ± 893	<LLD	109.6	27.4	0.053
Tabuhan	Entrance	0	286 ± 221	<LLD	8.9	2.2	0.004
	Room 1	60	1185 ± 419	<LLD	37.0	9.2	0.018
	Room 2A	80	1057 ± 198	<LLD	33.0	8.2	0.016
	Room 2B	90	1974 ± 450	<LLD	61.6	15.4	0.030
	Meditation room	100	2710 ± 404	<LLD	84.5	21.1	0.041
Semedi	Entrance 1	1	1735 ± 308	<LLD	54.1	13.5	0.026
	Water source	15	181 ± 83	<LLD	5.6	1.4	0.003
	Thin tunnel	25	254 ± 83	<LLD	7.9	2.0	0.004
	Exit door	30	222 ± 62	<LLD	6.9	1.7	0.003
	Entrance 2	35	124 ± 76	<LLD	3.9	1.0	0.002
Putri	Entrance	2	1793 ± 370	<LLD	56.0	14.0	0.027
	Room 1	15	2452 ± 700	<LLD	76.5	19.1	0.037
	Tunnel	30	1829 ± 280	<LLD	57.1	14.3	0.027
	Last room	40	1877 ± 317	<LLD	58.6	14.6	0.028
Kalak	Entrance	0	381 ± 108	604 ± 407	11.9	3.0	0.006
	Pesanggrahan	10	NA	NA	NE	NE	NE
	Meditation room	30	1639 ± 259	<LLD	51.1	12.8	0.025
	Shining rock	70	536 ± 244	<LLD	16.7	4.2	0.008
Dawung	Entrance	0	914 ± 241	<LLD	28.5	7.1	0.014
	Room 1	20	NA	NA	NE	NE	NE
	Room 2	100	1231± 238	<LLD	38.4	9.6	0.018
	Room 3	250	1495 ± 432	<LLD	46.7	11.7	0.022
Kendil	Entrance	0	1806 ± 939	<LLD	56.4	14.1	0.027
	Room 1A	5	2026 ± 547	5698 ± 3520	63.2	15.8	0.030
	Room 1B	30	1078 ± 224	<LLD	33.6	8.4	0.016
	Room 2	100	1358 ± 216	<LLD	42.4	10.6	0.020
Selo Arum	Entrance	1	450 ± 172	<LLD	14.0	3.5	0.007
	Hallway	30	1041 ± 263	<LLD	32.5	8.1	0.016
	Pawejangan	80	986 ± 186	<LLD	30.8	7.7	0.015
	Meditation room	100	636 ± 253	1527 ± 581	19.8	5.0	0.010
Somopuro	Entrance	2	NA	<LLD	NE	NE	NE
	Terrace	10	NA	<LLD	NE	NE	NE
	Room 1	30	NA	<LLD	NE	NE	NE
	Room 2	45	1716 ± 492	2545 ± 969	53.5	13.4	0.026
Jurug Jaran	Entrance	4	NA	NA	NE	NE	NE
	Near river	10	864 ± 268	<LLD	27.0	6.7	0.013
Laman	Point 1	3	7034 ± 458	5548 ± 1836	219.5	54.9	0.106
	Point 2	6	27,944 ± 1342	<LLD	871.9	218.0	0.419
	Point 3	12	29,893 ± 1426	<LLD	932.7	233.2	0.448
	Point 4	16	29,549 ± 1405	<LLD	921.9	230.5	0.443
X	Point 1	1	774 ± 287	<LLD	24.2	6.0	0.012
	Point 2	1.5	994 ± 227	1913 ± 899	31.0	7.8	0.015
	Point 3	2	1235 ± 469	<LLD	38.5	9.6	0.019

* Distance refers to distance of individual segment from entrance. <LLD = below the Lower of Limit Detection. NA = not available. NE = not estimated. Radon and thoron values are presented as mean ± measurement uncertainty.

Thoron was also detected at seven locations: Room 4 of Gong Cave, Entrance of Kalak Cave, Room 1A of Kendil Cave, Room 2 of Somopuro Cave, Point 1 of Laman

Cave, Meditation Room of Selo Arum Cave, and Point 2 of X Cave. At the remaining measurement locations, thoron concentrations were below the LLD. In Gong Cave, thoron was detected at only at Room 4 (6604 ± 1717 Bq·m^{-3}), where RADUET was positioned closer to the cave wall (26 cm) than at the other measurement points within the cave. At the six other caves where thoron was detected, the detectors were positioned directly on the cave walls (0 cm). In contrast, the distance of the detector to the wall at segments with thoron concentrations below the LLD varied, although most detectors were mounted directly on the cave walls. At Laman Cave, thoron was detected only at Point 1 near the entrance, whereas deeper measurement points showed thoron concentrations below the LLD despite higher radon concentrations. Overall, thoron detection occurred at specific locations and was not consistently associated with direct contact between the detectors and the cave walls.

The E_{in} also varied substantially among cave segments and exposure scenarios. Under the occupational worst-case scenario (2080 h year^{-1}), the highest doses occurred at Point 3 of Laman Cave 932.7 mSv year^{-1}, followed by Point 4 (921.9 mSv year^{-1}), Point 2 (813.7 mSv year^{-1}), and Point 1 (871.9 mSv year^{-1}). These were followed by Room 3 (206.0 mSv year^{-1}) and Room 2 (154.4 mSv year^{-1}) of Gong Cave. All measurement segments in Gong, Putri, Dawung, Kendil, Laman, and X Caves exhibited E_{in} values exceeding the ICRP occupational dose limit. Only one segment in Somopuro and Jurug Jaran Caves could be evaluated because the remaining detectors were lost but the available segments in both caves also exceeded the limit criterion. As under moderate-case scenario (520 h year^{-1}), doses at Laman Cave at Point 2–4 remained above the limit, ranging from 54.9 mSv year^{-1} to 233.2 mSv year^{-1}. Under this exposure scenario, all segments in Putri, Dawung, Kendil, and X Caves were below the recommended limit, while some segments in Gong Cave also fell below this limit. Overall, Semedi Cave had the lowest E_{in} (3.9 mSv year^{-1}) at Entrance 2 under a worst-case exposure scenario. Under public exposure (1 h year^{-1}), all investigated segments remained below the annual public dose limit of a 1 mSv year^{-1} public dose limit, with the highest E_{in} of 0.45 mSv year^{-1} at Laman Cave.

3.4.2. Ambient Dose Equivalent Rate $H^*(10)$ and External Effective Dose (E_{ex})

Mean of $H^*(10)$ varied spatially among investigated caves, as shown at Figure 4. In Gong Cave, values in Room 5–Room 7 were relatively homogeneous at 49–51 nSv h^{-1} (n = 9). Shallow caves, including Putri, Kalak, Dawung, Kendil, Somopuro, Jurug Jaran, Selo Arum, and X Caves have relatively homogeneous mean $H^*(10)$ values (n = 3). In Laman Cave, $H^*(10)$ increased from 45 nSv h^{-1} at the entrance to 259 nSv h^{-1} at Point 1 and increased further toward the deeper segments (n = 9). X Cave showed a smaller increase from 113 nSv h^{-1} at the entrance to 135 nSv h^{-1} at the 5 m from the entrance. In contrast, Gong Cave showed its highest $H^*(10)$ near the entrance, followed by a decrease and stabilization toward Room 7. Under the worst-case scenario, E_{ex} reached the highest values of 0.72 mSv year^{-1} at Point 2 and 0.64 at Point 4 of Laman Cave. X Cave showed higher E_{ex} outside of the entrance than inside, with a maximum of approximately 0.2 mSv year^{-1} (Table S10). Most other caves in various scenarios showed values below 0.72 mSv year^{-1}, which is consistent with spatial $H^*(10)$ values within each segment of cave.

From Table S8, the Kruskal–Wallis test showed significant spatial variations in $H^*(10)$ among segments, with the strongest differences observed in Gong Cave (H = 79.26, p = 5.72 × 10^{-12}), followed by Tabuhan Cave (H = 37.45, p = 1.44 × 10^{-6}) and Laman Cave (H = 36.68, p = 6.93 × 10^{-7}). Significant differences were found in the remaining caves. Dunn's post hoc tests showed that these differences were mainly associated with specific cave segments. In Gong Cave, $H^*(10)$ differed significantly between the entrance or Room 1 and deeper rooms, particularly Rooms 3–7. In Tabuhan Cave, significant differences were found between 10 m

from the entrance and entrance or Room 1, as well as between the entrance or Room 1 and Room 2B or the Meditation Room. In Laman Cave, significant differences occurred between 5 m from the entrance and Points 2–4, and between the entrance and Points 2–4. Thus, $H^*(10)$ was spatially heterogeneous within these caves. The Spearman rank correlation further showed that the relationship between $H^*(10)$ and distance from the cave entrance differed among caves (Table S9). Significant positive correlations were observed in Gong Cave ($\rho = 0.57$, $p = 0.04$) and Laman Cave ($\rho = 0.93$, $p = 0.01$), indicating that $H^*(10)$ tended to increase toward distance from the entrance. In contrast, a strong negative correlation was found in Kalak Cave ($\rho = -0.94$, $p = 0.005$) and Cave X ($\rho = -1.00$, $p < 0.001$), indicating that $H^*(10)$ tended to decrease toward distance from the entrance. No significant monotonic relationship was observed in Tabuhan, Semedi, Putri, Dawung, Kendil, Somopuro, Jurug Jaran, or Selo Arum caves. These results indicate that the spatial distribution of $H^*(10)$ varied among caves, with some caves showing a clear increase or decrease in $H^*(10)$ with distance from the entrance, while others showed significant differences between individual segments without a consistent relationship with distance.

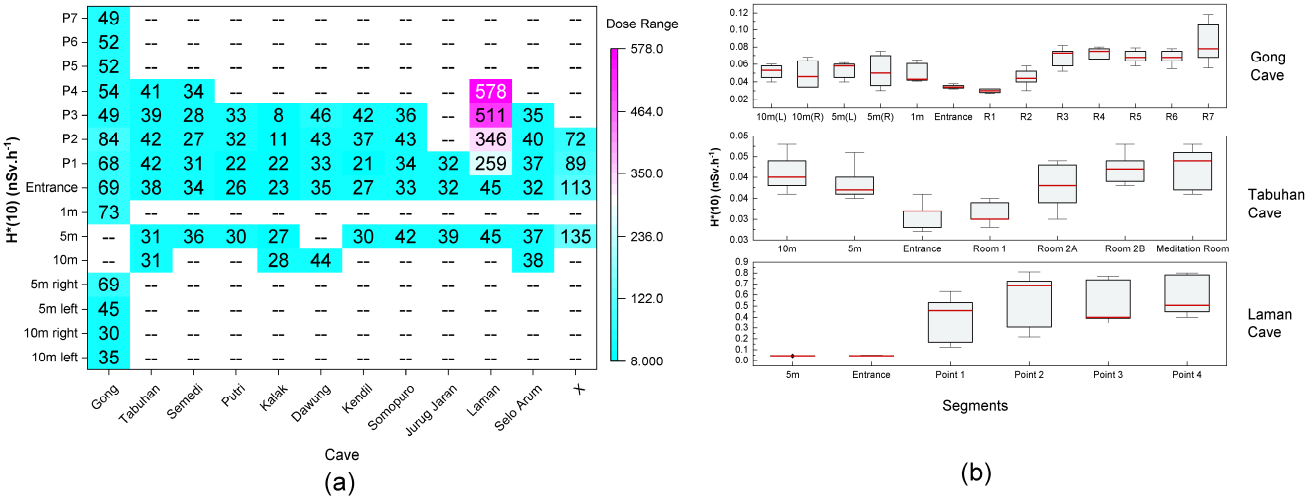

Figure 4. Spatial variation in mean ambient dose equivalent rate H*(10) across the investigated caves: (**a**) heatmap of ambient $H^*(10)$ measured at various segments across the investigated caves. Rows represent sampling segments from the cave exterior into the inner segments, whereas columns represent individual caves. Cell colors indicate the magnitude of $H^*(10)$. Blank cells indicate sampling segments which were not available in the cave. (**b**) Spatial variation in $H^*(10)$ across segments in the three representative caves: Gong, Tabuhan, and Laman Caves. Boxplot shows the median (red line), interquartile range (box), and minimum–maximum values.

3.4.3. Radiological Dose Assessment and Proposed Preliminary Zoning in Cave Mitigations

The estimated E_{total} varied among the investigated cave segments and occupancy scenarios (Table 8), indicating that potential annual exposure depended on both the measured radon activity concentration and the assumed occupational duration. The estimated E_{total} varied greatly; E_{in} was in the range of 98.92–99.97% and a small proportion of E_{ex} was in the range of 0.03–1.08%. Under the worst-case scenario, the majority of cave segments exceeded the 20 mSv·y^{-1} occupational criterion dose limit, with the highest E_{total} of 933.4 mSv·year^{-1} recorded in Laman Cave. The moderate-case scenario reduced the annual dose because of the shorter occupancy time, while the overall spatial pattern remained similar. Under the public exposure scenario, all annual effective doses were substantially lower and under the public recommendation limit of 1 mSv·y^{-1}.

Table 8. Estimated E_{total} for different exposure scenarios across the studied caves and estimated t_{max}. under the assumed exposure scenario.

Cave	Segment	E_{total} (mSv Year^{-1})			t_{max} (h Year^{-1})
		Worst Case	Moderate Case	Public	
Gong	Entrance	47.2	11.8	0.023	882.3
	Room 1	53.4	13.4	0.026	778.6
	Room 2	154.5	38.6	0.074	269.3
	Room 3	206.1	51.5	0.099	201.9
	Room 4	70.8	17.7	0.034	587.3
	Room 5	178.5	44.6	0.086	233.1
	Room 6	104.4	26.1	0.050	398.4
	Room 7	109.7	27.4	0.053	379.2
Tabuhan	Entrance	9.0	2.2	0.004	4633.8
	Room 1	37.0	9.3	0.018	1124.0
	Room 2A	33.0	8.3	0.016	1259.1
	Room 2B	61.6	15.4	0.030	675.0
	Meditation room	84.6	21.1	0.041	491.8
Semedi	Entrance 1	54.2	13.5	0.026	768.0
	Water source	5.7	1.4	0.003	7336.0
	Thin tunnel	8.0	2.0	0.004	5229.7
	Exit door	7.0	1.7	0.003	5967.9
	Entrance 2	3.9	1.0	0.002	10,678.3
Putri	Entrance	56.0	14.0	0.027	743.1
	Room 1	76.5	19.1	0.037	543.5
	Tunnel	57.1	14.3	0.027	728.4
	Last room	58.6	14.7	0.028	709.8
Kalak	Entrance	11.9	3.0	0.006	3491.7
	Pesanggrahan	0.03 *	0.008 *	2×10^{-5} *	NE
	Meditation room	51.2	12.8	0.025	813.1
	Shining rock	16.7	4.2	0.008	2485.7
Dawung	Entrance	28.5	7.1	0.014	1457.3
	Room 1	0.04	0.010	2×10^{-5} *	NE
	Room 2	38.5	9.6	0.018	1081.6
	Room 3	46.7	11.7	0.022	890.5
Kendil	Entrance	56.4	14.1	0.027	737.8
	Room 1A	63.2	15.8	0.030	657.8
	Room 1B	33.7	8.4	0.016	1234.8
	Room 2	42.4	10.6	0.020	981.0
Selo Arum	Entrance	14.1	3.5	0.007	2956.8
	Hallway	32.5	8.1	0.016	1279.5
	Pawejangan	30.8	7.7	0.015	1349.5
	Meditation room	19.9	5.0	0.010	2092.3
Somopuro	Entrance	0.042 *	0.010 *	2×10^{-5} *	NE
	Terrace	0.042 *	0.011 *	2×10^{-5} *	NE
	Room 1	0.054 *	0.013 *	3×10^{-5} *	NE
	Room 2	53.6	13.4	0.026	776.3
Jurug Jaran	Entrance	0.040 *	0.010 *	2×10^{-5} *	NE
	Near river	27.0	6.7	0.013	1540.8
Laman	Point 1	219.5	54.9	0.106	189.5
	Point 2	872.4	218.1	0.419	47.7
	Point 3	933.4	233.3	0.449	44.6
	Point 4	922.6	230.6	0.444	45.1
X	Point 1	24.3	6.1	0.012	1711.9
	Point 2	31.1	7.8	0.015	1336.7
	Point 3	38.6	9.7	0.019	1077.2

* The E_{total} for these segments only reflects the external effective dose (E_{ex}) and represents a lower-bound estimate, as the internal radon contribution could not be quantified. NE, not estimated; because radon measurement is unavailable, the corresponding estimated maximum occupancy time could not be reliably assessed.

The estimated maximum allowable annual occupancy times (t_{max}, h y^{-1}) are proposed as preliminary screening estimates to inform cave-management decisions. The maximum occupancy duration was calculated for cave workers under both worst-case and moderate-

case scenarios. The estimated t_{max} increased as the estimated E_{total} was decreased, indicating that t_{max} calculations could serve as one of the bases for planning worker rotation schedules to manage occupational radiation exposure in tourist caves. These values depend on the assumed dose criterion and should not be interpreted as established safe occupancy durations, because actual exposure depends on the stay duration in different cave segments and variations in radon concentrations. Based on the measured radon concentrations, estimated annual effective doses, and assumed occupancy durations, preliminary site-specific radiation management zones for investigated cave segments are proposed in Figure 5. These classifications indicate further review of occupancy durations; they do not represent formal regulatory designations.

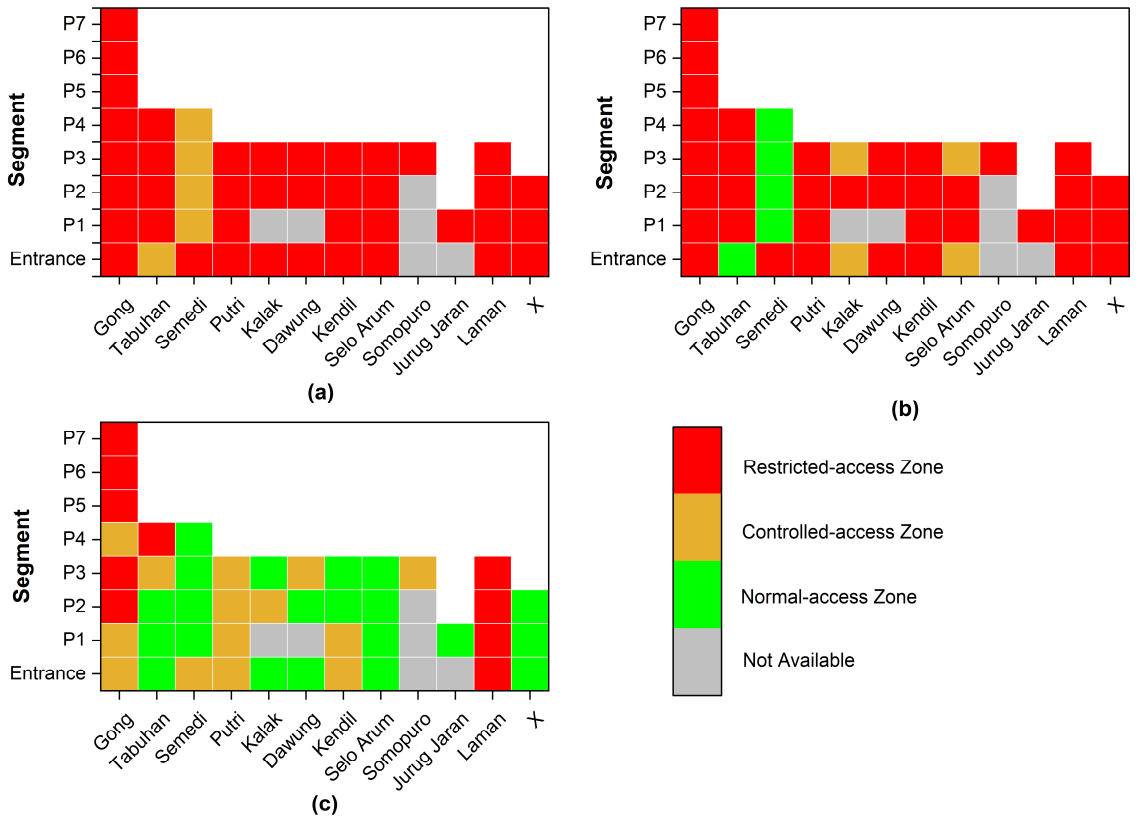

Figure 5. Proposed cave access-zone classifications across 12 caves based on (**a**) radon concentrations, (**b**) annual effective dose under worst-case scenario, and (**c**) annual effective dose under moderate-case scenario. White cells represent cave segments without sampling locations.

Under the worst-case scenario, 36 of the 45 classified cave segments (80.0%) were designated as restricted-access zones, while 4 (8.9%) and 5 (11.1%) segments were classified as controlled-access and normal-access zones, respectively. Under the moderate-case scenario, the number of restricted-access segments decreased substantially to 9 (20.0%), whereas controlled-access and normal-access segments increased to 15 (33.3%) and 21 (46.7%), respectively. A segment-level comparison between the two exposure scenarios revealed that 31 of the 45 classified segments (68.9%) shifted to less restricted-access categories. Specifically, 12 segments changed from restricted to normal-access, 15 from restricted to controlled-access, and four from controlled to normal-access. The remaining 14 segments retained their original classifications, comprising nine restricted-access and five normal-access segments. The nine segments that remained classified as restricted-access zones were located exclusively in Gong (four segments) and Laman (four segments) Caves.

4. Discussion

Radon concentrations in Gong Cave remained consistently high, with moderate short-term fluctuations and no clear diurnal cycle (Figure 3a). The limited difference between daytime and nighttime concentrations suggests weak air exchange and limited influence of external atmospheric conditions [23]. This behavior is probably associated with the multi-level morphology of Gong Cave, where the complex internal geometry limits direct air exchange and promotes radon accumulation. The nearly constant temperature and persistently high relative humidity further indicate a stable cave microclimate. Although five blowers are installed, they primarily promote internal air circulation rather than direct exchange with the outside atmosphere. Thus, continuous mechanical airflow may reduce the influence of natural diurnal ventilation, which may be insufficient to prevent radon accumulation. The lack of correspondence between radon and RH or air pressure further suggests that these parameters had limited influence on short-term radon fluctuations under the prevailing ventilation conditions.

According to Figure 3b, Laman showed a highly confined microclimatic system, with radon concentrations ranging from 60,000 to 70,000 Bq m^{-3}, temperature varying by less than 0.5 °C, and RH increasing from approximately 89% to 96%. Pressure fluctuations were not accompanied by corresponding changes in radon concentration, suggesting that short-term weather variations had only a limited influence on cave-air replacement over the monitoring period [23,63]. The persistently high concentration was therefore likely controlled primarily by restricted ventilation associated with Laman's vertical and confined morphology. Under such conditions, continuous emanation of ^{222}Rn from ^{226}Ra in the ^{238}U decay chain series can maintain high concentrations when air exchange is limited [64]. This interpretation is consistent with previous findings that cave morphology and ventilation efficiency are the main factors controlling radon accumulation in confined karst systems [14,65], while short-term environmental fluctuations play a secondary role under highly restricted ventilation conditions [13,66].

According to the geological map and Table 1, GIS analysis showed that Laman Cave is located within Jaten Formation, which comprises conglomerate, conglomeratic sandstone, tuffaceous sandstone, mudstone, lignite, carbonaceous shale, and tuff, with locally sulphury characteristics. The surrounding geological units include the Arjosari Formation, which contains sedimentary and volcanic rocks, and the Wuni Formation, which comprises volcanic breccia, tuff, tuffaceous sandstone, lithic sandstone, and siltstone, with intercalations of lignite and limestone and locally occurring blocks of silicified wood. GIS placed Laman Cave approximately 288 m from the Kayuwayang Fault, 210 m from the nearest contact associated with the Arjosari Formation, 1129 m from the nearest Wuni Formation contact, and 747 m from Tomi (4) intrusive body. These geological features provide a framework for evaluating potential radon sources and subsurface gas migration pathways.

Faults and associated fractures may facilitate radon transport by increasing secondary permeability and connecting radon-bearing geological materials with underground cavities [67,68]. Geological discontinuities may provide pathways for radon-bearing gases, while restricted air exchange promotes accumulation inside the cave [13,69]. However, faults should be considered potential migration pathways rather than confirmed radon sources unless their radionuclide content and gas transport characteristics are independently established. The relative positions of the eastern cluster indicate that proximity to a single geological feature cannot explain the exceptionally high radon concentration in Laman Cave. Jurug Jaran Cave is closer to the Kayuwayang fault, while X Cave is closer to both the Tomi (4) and lithological contact. Therefore, Laman is not the closest cave to any of the three mapped geological features. This comparison suggests that faults, intrusive bodies, and lithological contacts may influence the potential supply and transport of radon

supply and transport pathways. However, their proximity should not be interpreted but their effects cannot be inferred from distance alone.

The high radon concentration in Laman is likely controlled by the combined effects of radon accumulation, subsurface transport, and limited ventilation. The cave morphology is consistent with Laman having a single, narrow entrance, and the investigated segment is classified as a confined chamber. This configuration may limit air exchange between the cave interior and the external atmosphere, although the degree of ventilation limitation cannot be determined from morphology alone. Field observations provide additional qualitative evidence of potentially poor air exchange. The deeper part of Laman is noticeably hot and stuffy, CO_2 concentration exceeded the upper measurement limit, and an open flame was extinguished shortly after entering the deeper section. These observations indicate poor air exchange and limited ventilation but do not establish the direction or mechanism of airflow. O_2 and airflow velocity were not measured directly.

Because ^{226}Ra concentrations in the host rock, surrounding geological units, cave sediments, and overlying deposits were not measured, the dominant radon source cannot be identified, and the relative contributions of the surrounding bedrock and possible Quaternary deposits remain uncertain. Although temperature was monitored and showed temporal fluctuations during the observation period, these measurements alone do not establish whether temperature drove convective air movement. Simultaneous temperature measurements at different heights or locations, together with direct airflow measurements, would be needed to evaluate this mechanism. The exceptionally high radon concentration in Laman Cave is therefore most reasonably interpreted as potentially resulting from the interaction between radon supply, geological transport pathways, and morphology-related restrictions on air exchange, rather than from proximity to any single mapped geological feature.

Unlike Gong and Laman Caves, Tabuhan Cave showed more dynamic temporal variations in ^{222}Rn and CO_2 (Figure 3c), indicating the cave atmosphere remained responsive to short-term environmental changes. Radon concentrations reached 2100–2200 Bq m^{-3} on the afternoon of Day 2 and subsequently decreased until reaching its lowest value at the end of Day 3, indicating enhanced air-exchange dan dilution. There was a significant positive correlation between radon and CO_2 ($\rho = 0.536$, $p < 0.0001$), suggesting that both gases responded simultaneously to ventilation changes despite different sources [70–72]. Changes in ventilation may therefore affect the accumulation and dilution of both gases simultaneously. Relative humidity reached 99% and remained relatively stable, suggesting that it was not the primary factor controlling short-term radon fluctuations. Otherwise, the temperature increased from 25.2 °C to 25.6 °C around the 42nd hour, and the pattern of atmospheric pressure fluctuations coinciding with changes in gas concentrations suggests possible changes in air movement during the monitoring period. However, because the ventilation rate was not directly measured, this relationship is more appropriately interpreted as an indication that external atmospheric conditions and cave characteristics influence gas dynamics, with sufficient connection to the outside atmosphere for periodic air exchange but allowing ^{222}Rn and CO_2 accumulation under lower air exchange conditions. Thus, ventilation dynamics contribute to both temporal radon fluctuation and the spatial accumulation of ^{222}Rn and CO_2 in Tabuhan Cave.

The temporal pattern was further supported by the spatial distribution of passive radon measurement, ranging widely from 181 to 71,003 Bq m^{-3} (Table 3). The highest concentration exceeded those reported in several tropical karst cave studies in the Philippines, Mexico, Vietnam, Brazil, and Cuba [27–34], but remained below the maximum concentrations reported in Venezuela [35] (Tables S10 and S11). Compared with selected non-tropical karst caves, the maximum concentration in Pacitan was higher than these reported studies in Spain and Slovakia but lower than that reported in Southwestern China [14,73,74]. Previ-

ous studies have suggested that geological materials, cave morphology, rock fractures, and ventilation may contribute to differences in radon concentrations. For instance, ventilation related to cave entrances was proposed as a factor in Philippine caves, while geological features and seasonal ventilation were discussed in Rong Cave, Vietnam. Although the investigated caves share broadly tropical climatic conditions, differences in cave morphology and local ventilation may contribute to the observed variation in radon concentrations.

The geological comparison in Table S11 also shows that radon concentrations in tourist caves in the Philippines, Malaysia, and Jamaica are developed in limestone, similar to the carbonate rocks found in the Pacitan study area. As shown in Table 1, the Wonosari Formation in Pacitan consists of few types of limestones. Similar carbonate lithologies have been reported in the Philippine caves, while studies in Vietnam and Ecuador describe limestone associated with clay-rich or other sedimentary materials. However, the Pacitan study area also includes volcanic, volcaniclastic, intrusive, and clastic sedimentary rocks. The western cave cluster is located within a more heterogenous geological setting, whereas the eastern cluster is predominantly associated with the Jaten Formation, with nearby faults, lithological contacts, and intrusive bodies. Despite some similarities in lithology, radon concentrations vary considerably among the investigated regions, suggesting that lithology alone cannot explain the observed differences. The contribution of other factors including radionuclide content, geological structures, rock permeability, and cave ventilation may also influence radon concentrations. However, their individual contributions remain uncertain without direct geological and radionuclide measurements.

The RADUET detectors were hanging on cave walls, making local thoron emanation from nearby surfaces a possible influence on the measured concentrations. Thoron has a short half-life of approximately 55.6 s, and its concentrations can vary over short distances and areas strongly depending on surface exhalation and air movement [54,75,76]. This spatial variability is particularly evident at Laman Cave, where thoron was detected only at Point 1 near the entrance, while radon concentrations increased substantially at the deeper measurements point while thoron remained below the lower LLD. But measurements below the detection limit should not be interpreted as proof of thoron absence. This contrast is consistent with the different half-lives and transport characteristics of the two isotopes. The detection pattern across caves with different morphologies, including the open, low-ceiling chamber of X Cave and the chamber with lentic environment at Somopuro Cave, suggests that morphology alone cannot explain thoron distribution. However, because the radionuclide content of the surrounding materials and local airflow were not measured, the contributions of surface emanation and ventilation remain uncertain.

Particulate matter (PM) measurements were conducted only in Gong Cave as supplementary observations to provide information on local aerosol conditions. They were not a key parameter in this study and were not used in the effective dose calculations or cave access classifications. The PM concentrations were generally highest near the cave entrance and generally decrease toward inner segments, indicating spatial variation in aerosol distribution that may be associated with air exchange and local environmental conditions [77–79]. A significant negative correlation was observed between RH and the fine PM fractions (Figure S3), while no significant correlation was found between temperature and any PM fractions. Although airborne particles may influence the attachment and behavior of radon progeny, PM concentrations alone cannot be used to determine their contribution to internal dose [79]. Further measurements of PM and radon progeny across multiple caves are needed to understand their relationship and potential implications for internal dose estimations.

According to Table 7, the spatial variation in internal effective dose (E_{in}) closely followed the distribution of ^{222}Rn concentrations, confirming that radon concentration was the

primary factor determining inhalation exposure in the investigated caves. Room 3 of Gong Cave (6603 Bq m^{-3}) and the inner sections of Laman Cave (> 27,000 Bq m^{-3}) exhibited substantially higher internal doses than all other investigated sites. This proportional relationship indicates that radiological exposure is strongly influenced by radon concentrations and occupancy [38,54]. Under the worst-case occupational scenario, internal effective doses at several locations in Laman Cave exceeded the ICRP recommended occupational limit 20 mSv $year^{-1}$, which indicates significant radiological concern for cave personnel [25]. In contrast, all estimated doses under the public exposure scenario remained below the public dose limit of 1 mSv $year^{-1}$, suggesting substantially lower exposure for a short duration.

The radon equilibrium factor (F_{eq}) represents an important source of uncertainty in estimating the internal effective dose (E_{in}), as it represents the ratio of equilibrium-equivalent radon gas and its short-lived progeny. ICRP Publication 137 uses F_{eq} = 0.4 as a reference value for tourist caves, while Commission also acknowledges that F_{eq} can vary with values of approximately 0.2–0.5 for cave environments [38]. Chen and Harley (2020) reviewed measurements from 136 show caves, tourist mines, and thermal spas, reporting F_{eq} values ranging from 0.10 to 0.85, with a weighted mean of 0.39, which is close to the default value used in this study [80]. However, substantial variation among these measurements suggests that a single equilibrium factor may not adequately represent all caves, particularly where ventilation, aerosol concentrations, and radon progeny behavior differ. Therefore, although F_{eq} = 0.4 was retained as the baseline assumption in this study, its potential influence on dose estimation and the resulting management classifications were examined through a sensitivity analysis.

The sensitivity analysis (%Δ E_{in}) presented in Table S13 shows that the estimated internal dose depends strongly on the assumed F_{eq}. Relative to the baseline value of 0.4, using F_{eq} to 0.2 and 0.5 changes the estimated internal dose by −50%, and +25%, respectively. The value of 0.2 was used as a lower-factor scenario, while 0.5 represents the upper limits of the mean F_{eq} by ICRP Publication 137. These values provide literature-based sensitivity scenarios rather than site-specific estimates for Pacitan caves. Under the worst-case scenario, all measured segments in Gong Cave were above the occupational dose criterion of 20 mSv·y^{-1} at F_{eq} = 0.4; but they decreased 50% when the effective doses were incorporated by F_{eq} = 0.2 but remained above the occupational dose criterion of 20 mSv·y^{-1}. Under the moderate-case scenario, Room 3 and Room 5 exceeded the dose criterion at F_{eq} = 0.2, whereas the remaining rooms were below this criterion, but they exceeded the dose criterion at F_{eq} = 0.2. In contrast, estimated doses in all segments of Laman Cave remained in the hundreds of mSv·y^{-1} across the tested equilibrium factors and occupancy scenarios. Under the public scenario, all estimated doses were below the public dose criterion of 1 mSv·y^{-1}. These findings indicate that occupational dose classifications in Gong Cave may be sensitive both to the assumed F_{eq} and t_{occ}, whereas Laman Cave remains a priority for exposure management even under F_{eq} assumptions. Therefore, the estimated dose exceedances should be interpreted as scenario-dependent screening results rather than confirmed occupational exposures.

The assumption of a uniform F_{eq} may also overlook spatial differences in radon progeny equilibrium within individual caves. Ventilation, aerosol characteristics, relative humidity, and the deposition of radon progeny on surrounding surfaces may influence the relationship between radon gas and its short-lived progeny [80–82]. Consequently, conditions in deeper or poorly ventilated sections may differ from those near cave entrances, although the magnitude and direction of these differences cannot be established from the present measurements. Direct measurements of radon concentration and equilibrium-equivalent concentration (EEC) at multiple segments are therefore needed to determine whether spatial variations in F_{eq} could affect dose estimations or management classifications.

Indonesia's tropical climate is generally characterized by relatively small seasonal variations in temperature (~3 °C) and humidity (70–90% band) throughout the year [83,84]. According to climate observations at Pacitan Station in 2025, monthly mean of outdoor temperatures ranged from 28.8 to 32.5 °C while monthly mean of RH remained high, ranging from 88.42% to 94.78%. However, rainfall frequency varied throughout the year, with 6–7 rainy days per month during July–September and 21–24 rainy days per month during November–January [85]. A paired t-test found no significant difference in ^{222}Rn between seasonal in indoor radon between the dry and rainy seasons (p = 0.45); mean indoor radon was stable (≈1.7 mSv annual dose, largely unchanged by season) [18]. We expected similarly limited seasonal radon swings on average due to the small T/H variation, but with potential short-term peaks during rains if cave ventilation changes. Unlike caves in regions with a four-season climate such as in Slovenia, Poland, and Slovakia, where seasonal radon variations are often associated with temperature-driven ventilation [66,74,86], tropical caves may exhibit different seasonal patterns due to regional climatic conditions, rainfall, and cave-specific characteristics. Although the relatively limited variations in outdoor temperature and humidity in Pacitan may influence seasonal patterns inside the cave, they do not guarantee no significant seasonal variations of radon concentrations in the cave. Rainfall in soil and cave ventilation may also contribute to short-term radon fluctuations. Continuous seasonal monitoring of radon with microclimatic measurements is recommended to better characterize seasonal variations and improve the reliability of internal effective dose estimates.

The measured $H^*(10)$ in Figure 4a showed clear spatial heterogeneity among the investigated caves. While most caves exhibited low and relatively uniform dose rates, a marked increase was observed in deeper sections of Laman Cave, reaching 578 nSv·h^{-1} at Point 3 and Point 4. This increase may reflect differences in naturally occurring radioactive materials (NORMs) within the surrounding rocks, sediments, and soils [87]. However, short-lived ^{222}Rn progeny, particularly ^{214}Pb and ^{214}Bi, also emit gamma radiation and can contribute to the external dose rate when their concentrations are high [88,89]. The higher $H^*(10)$ values near and outside the cave entrance are more likely associated with local lithological variations in the rock's formation. However, the specific radionuclides contributing to this increase cannot be identified without gamma spectrometry analysis of soil and rock samples to determine their radionuclide activity concentrations.

A different pattern was observed at X Cave. Despite its closer position to both the nearest Tomi intrusive body, lithological contact, and Kayuwayang Fault, the $H^*(10)$ decreased toward the cave interior, while a higher value was recorded outside the entrance. This pattern suggests that the external gamma field at X Cave may be influenced by local geological heterogeneity. The combination of intrusive rocks, lithological boundaries and structural features may produce spatial variations in the distribution of naturally occurring radioactive materials within surface soils, weathered rocks, and exposed bedrock.

The higher $H^*(10)$ outside may therefore reflect stronger terrestrial gamma contributions from near-surface geological materials. In contrast, the lower values inside the cave may result from changes in source geometry and increased shielding by the surrounding rock mass. However, because gamma spectrometry and radionuclide measurements were not performed, the specific geological material or radionuclide for this pattern cannot be identified. Thus, the X Cave anomaly is better interpreted as a local variation in the terrestrial gamma radiation within a geologically heterogenous setting, rather than as a direct effect of radon or proximity to a single mapped geological feature. Despite this spatial variation, the E_{ext} remained minor, below 0.3 mSv·y^{-1}, even under the worst-case occupational scenario.

Overall, E_{total} was dominated by radon inhalation [90], while the contribution of $H^*(10)$ contributed less than 2% (Table 4). The spatial distribution of E_{total} closely followed that of E_{in}, particularly in sections where restricted air exchange promoted persistent radon accumulation. These findings indicate that internal exposure was the main contributor to the estimated total dose during monitoring. However, measurements were conducted only during January–February 2026 and may not represent year-round conditions. Therefore, the annualized dose estimates and their spatial patterns should be interpreted as conditional scenarios rather than validated annual exposure estimates. Longer-term monitoring across different seasons, together with direct ventilation measurements, is needed to better characterize temporal variations in exposure. Meanwhile, radiological protection in Pacitan caves should prioritize radon monitoring while also considering external gamma radiation and seasonal variability.

Practical radiological protection in caves should follow the principle of optimization, commonly expressed as As Low As Reasonably Achievable (ALARA), through routine radon monitoring, occupancy-time management, work rotation, and localized ventilation improvements where necessary [55,71]. The t_{max} helps translate these screening assessments into practical management priorities. The particularly short estimates in Laman Cave (47.8–203.0 h year^{-1}) and restricted segments in Gong Cave (216.3–426.8 h year^{-1}) support stricter access controls and reduced occupational occupancy. In normal-access zones, periodic radon monitoring and preservation of natural ventilation conditions are suggested [26,55,56,61]. Controlled-access zones require limited occupancy times, work rotation, and more frequent monitoring (semi-annual to quarterly) [26,56,61,62,91] while restricted-access zones should be reserved for essential activities involving short-duration entry, individual exposure assessment, and carefully evaluated ventilation interventions [14,26,28,61,62,71].

The implications of prolonged radon exposure further support the need for radiation dose assessment. Radon-related cancer risk can be assessed using epidemiological data, while dose-based risk estimates can also be applied [92]. Lung cancer is associated with exposure to radon and short-lived radon progeny, with risk increasing with prolonged exposure [20]. Inhaled radon progeny emits alpha particles that can damage cell and DNA and contribute to lung carcinogenesis. The risk of lung cancer increases about 16% for every 100 Bq m^{-3} increase in radon concentration [93]. Therefore, high radon concentrations and internal effective dose in several cave segments, especially under long-term occupational exposure, should be considered indicators of potential health risk associated with prolonged occupancy. These findings highlight the importance of routine radiation monitoring, exposure-duration management, monitoring of microclimatic parameters in cave environment, and characterization of radon and progeny in caves where occupants may spend prolonged period inside.

Future research should strengthen this framework through measurement of site-specific F_{eq} values, radon progeny concentrations, and ventilation rates to improve the accuracy of dose estimation in tourist karst caves and provide a stronger baseline for radiological management of tourist caves in tropical environment, particularly in Indonesia. Characterization of natural radioactivity in cave rocks, soils, and sediments, together with radon exhalation measurements, would help distinguish local geological radioactivity from radon transport and accumulation, particularly at the radiological hotspot in Laman Cave. Radon measurements in river water from Jurug Jaran Cave are also recommended because the water is used by local communities for drinking and domestic purposes and may represent an additional exposure pathway through ingestion. Finally, surveys of actual occupational occupancy durations are recommended to support more specific zoning and mitigation measures.

5. Conclusions

This study identified substantial variations in radon concentrations across the investigated tourist caves, highlighting potentially high-exposure locations during the monitoring period. The estimated annual effective doses and scenario-based access classifications suggest that occupancy duration is an important consideration for managing radon exposure, particularly for cave workers. However, these estimates are subject to uncertainties associated with temporal radon variability, radon equilibrium factor, occupational duration assumptions, and dose conversion parameters. Therefore, the proposed access zones and maximum allowable occupancy times should be regarded as preliminary screening and management tools rather than validated year-round recommendations or established safe exposure limits. Further verification of dose calculations, long-term radon monitoring across different seasons, and site-specific occupational exposure assessments are necessary before implementing definitive access restrictions and occupancy guidelines. Nevertheless, the findings provide a useful basis for prioritizing radon monitoring and developing precautionary radiation strategies in Indonesian tourist caves.

Supplementary Materials: The following supporting information can be downloaded at: https://www.mdpi.com/article/10.3390/environments13120640/s1, Figure S1: Flowchart for dose assessment in cave environment; Figure S2: Logarithmic graph of spatial distribution and variability of particulate matter (PM) concentrations across different segments in Gong Cave; Figure S3: Spearman rank correlation analysis among PM fractions and environmental parameters in Gong cave; Figure S4: Spatial variation in passive radon concentration along the segments in representative studied caves; Table S1: Study Area of Measurement; Table S2: Morphology Profile of Investigated Caves; Table S3: RADUET deployment in Pacitan study area; Table S4: Mean concentration of $PM_{0.3}$, $PM_{0.5}$, $PM_{1.0}$, $PM_{2.5}$, $PM_{5.0}$, and $PM_{10.0}$ in Gong cave; Table S5: Normality Shapiro–Wilk test of $PM_{0.3}$, $PM_{0.5}$, $PM_{1.0}$, $PM_{2.5}$, $PM_{5.0}$, $PM_{10.0}$, Temperature, and Relative Humidity in Gong cave; Table S6: Normality Shapiro–Wilk test of radon distribution in studied karst cave; Table S7: Spearman Rank correlation analysis of spatial radon distribution in studied karst caves in Pacitan; Table S8: Results of overall group comparison (Kruskal-Wallis test and Dunn's post hoc) for H*(10) among segments in studied caves; Table S9: Spearman Rank correlation analysis of spatial H*(10) distribution in studied karst caves in Pacitan; Table S10: Calculated annual external effective doses (E_{ext}) for different exposure scenarios across the studied caves; Table S11: Comparison of radon concentrations and radiation dose assessments in tropical and selected non-tropical tourist karst caves; Table S12: Geological/Karst settings of selected tourist caves and their reported implications for radon; Table S13: Estimated E_{in} under different time occupancy (t_{occ}) scenarios using the conventional F_{eq} = 0.2 and alternative values reviewed by [80].

Author Contributions: Conceptualization, E.D.N. and S.T.; methodology, E.D.N.; software, F.A.A., K.A., W., A.N.R. and M.M.F.; validation, E.D.N., J.A.E.N., S.T., C.K. and O.B.M.; formal analysis, F.A.A. and R.P.; investigation, F.A.A., Y.E., K.A., A.T.D., N.A., W., M.M.F. and R.P.; resources, E.D.N., C.K., O.B.M., W., A.N.R. and M.M.F.; data curation, F.A.A., Y.E., A.T.D. and N.A.; writing—original draft preparation, F.A.A.; writing—review and editing, F.A.A., J.A.E.N., Y.E., K.A., N.A., A.T.D., W., A.N.R., M.M.F., R.P., S.T., C.K., O.B.M. and E.D.N.; visualization, F.A.A., A.T.D., N.A. and A.N.R.; supervision, E.D.N. and J.A.E.N.; project administration, F.A.A., Y.E. and K.A.; funding acquisition, E.D.N., C.K. and O.B.M. All authors have read and agreed to the published version of the manuscript.

Funding: This research was funded by BRIN-RIIM No. RIIM-16 by National Research and Innovation Agency (BRIN), Indonesia Endowment Funds for Education (LPDP), ERAN-I-26-26 by ERAN Japan.

Data Availability Statement: All data generated or analyzed during this study are included in this published article (and its Supplementary Material file).

Acknowledgments: The authors gratefully acknowledge the Department of Tourism, Culture, Youth, and Sports of Pacitan Regency and the village heads of the respective cave localities for providing administrative permission and logistical support. Special thanks are also extended to the cave caretakers and local cave workers for their invaluable assistance, guidance and coordination during the fieldwork and data collection. The authors also gratefully acknowledge the LPDP for providing scholarship support. Finally, the authors thank Anderson Donovan Aaron of Institute of Radiation Emergency Medicine, Hirosaki University, Japan, for carefully proofreading and editing the English text of this manuscript.

Conflicts of Interest: The authors declare no conflicts of interest.

Appendix A. Derivation of the Maximum Allowable Occupancy Time (t_{max})

Appendix A.1. Specific Derivation of t_{max}

The committed effective dose concept described in ICRP Publication 147 considers the accumulation of dose following an intake over time [92]. In this study, the same time-integration principle was applied to estimate effective dose accumulated during occupancy in a cave. Equation (A1) expressed the fundamental principle that cumulative dose is the time integral of dose rate [94]. Assuming that the estimated effective dose associated with radon concentration and ambient dose equivalent rate remained constant, or were represented by their average values during exposure period, Equation (A2) is derived from differentiating Equation (A1).

$$E = \int_0^t \dot{E}(t) \cdot dt \tag{A1}$$

$$E = \dot{E} \cdot t \tag{A2}$$

$$E_{in} = \dot{E}_{in} \cdot t \text{ and } E_{ex} = \dot{E}_{ex} \cdot t$$

where $E(t)$ is the time-dependent effective dose rate (mSv·h^{-1}), $\dot{E}_{in}$ is the internal effective dose rate from radon inhalation (mSv·h^{-1}), and $\dot{E}_{ex}$ is the external effective dose rate from gamma radiation (mSv·h^{-1}).

Accordingly, the effective dose from internal exposure and from external exposure are given by the following:

$$E_{in} = \dot{E}_{in} \cdot t_{occ} \tag{A3}$$

$$E_{ex} = \dot{E}_{ex} \cdot t_{occ} \tag{A4}$$

Equations (A3) and (A4) substituted into Equation (9). The Equation (A5) is differentiated with respect to time.

$$E_{total} = \left(\dot{E}_{in} + \dot{E}_{ex}\right) \cdot t_{occ} \tag{A5}$$

$$\dot{E}_{total} = \dot{E}_{in} + \dot{E}_{ex} \tag{A6}$$

$$E_{total} = \dot{E}_{total} \cdot t_{occ} \tag{A7}$$

The t_{max} is obtained by setting the accumulated total effective dose at t_{max} is equal to the applicable reference dose.

$$E_{ref} = \dot{E}_{total} \cdot t_{max} \tag{A8}$$

$$t_{max} = \frac{E_{ref}}{\dot{E}_{total}} \tag{A9}$$

$$t_{max} = \frac{E_{ref}}{\dot{E}_{in} + \dot{E}_{ex}} \tag{A10}$$

Because the E_{total} was calculated over the assumed occupancy period (t_{occ}), the corresponding average total effective dose rate from Equation (A7) is obtained as Equation (A11). Therefore, the estimated t_{max} is as shown at Equation (10).

$$\dot{E}_{total} = \frac{E_{total}}{t_{occ}} \tag{A11}$$

where $\dot{E}_{total}$ is the total effective dose rate ($mSv \cdot h^{-1}$), and E_{ref} is the selected screening reference dose ($mSv \cdot y^{-1}$).

Appendix A.2. Derivation of the Independence of t_{max} from Annual Occupancy Time

The calculated total effective dose depends on the assumed annual occupancy time (t_{occ}), so the relationships between t_{max} and t_{occ} were further examined. If we are using Equation (A7) for substituting into Equation (10), t_{occ} cancels during the derivation, indicating that t_{max} is determined by the effective dose rate and the reference dose level, rather than by the assumed annual occupancy time.

$$t_{max} = \frac{E_{ref} \cdot t_{occ}}{E_{total}} = \frac{E_{ref} \cdot \ t_{occ}}{\dot{E}_{total} \cdot t_{occ}} = \frac{E_{ref}}{\dot{E}_{total}} \tag{A12}$$

Equation (12) can be demonstrated using a case study in Gong Cave, where the estimated effective dose at the entrance was 47.2 $mSv \cdot y^{-1}$ under the worst-scenario and 11.8 $mSv \cdot y^{-1}$ under the moderate scenario. Using a reference dose limit (E_{ref}) of 20 $mSv \cdot y^{-1}$ and the corresponding t_{occ} for each scenario, the calculated t_{max} values were identical, confirming that t_{occ} does not affect t_{max}.

References

1. Ermawati, K.C.; Sari, J.A. Potensi Obyek Wisata Goa Gong, Pantai Klayar, Pemandian Air Panas Tirta Husada di Kabupaten Pacitan. *J. Pariwisata Indones.* **2014**, *10*, 103–113.
2. Setyaji, G.W.; Haryono, E. Carbon dioxide variability in Gong Cave, Pacitan Regency, Indonesia. *IOP Conf. Ser. Earth Environ. Sci.* **2020**, *451*, 012094. [CrossRef]
3. Kusumayudha, S.B.; Setiawan, J. Identifikasi Keanekaragaman Geology untuk Mendukung Daerah Gunungsewu Sebagai Kawasan Geopark Dunia. *JIK TekMin* **2011**, *24*, 75–85.
4. Sumarmi; Meiji, N.H.P.; Purwasih, J.H.G.; Kodir, A.; Andriesse, E.H.S.; Ilies, D.C.; Miichi, K. Development, Social Change and Environmental Sustainability. In *Contemporary Sociology and Educational Transformation (ICCSET)*; CRC Press/Balkema: Malang, Indonesia, 2021.
5. Wahyudiono, S. Increasing the Tourists' Revisit Intention by Paying Attention to Tourist Satisfaction at the Gong Cave Pacitan Tourist Destination. 2022. Available online: http://ojs.stiami.ac.id (accessed on 12 April 2026).
6. Hawa Nurjannah, S.; Adam Hilman, Y.; Triono, B. The Development Of Goa Tabuhan And Its Impact In Pacitan Regency. *J. Partisipatoris* **2020**, *2*, 42–50. [CrossRef]
7. Hilman, A.Y. Pemenuhan Unsur Pokok Dalam Pengembangan Destinasi Wisata Goa Tabuhan Kabupaten Pacitan. *Epigram* **2021**, *18*, 71–79. [CrossRef]
8. Wulandari, R.; Budiyono, B.; Sulistiyani, S.; Wahyuningsih, N.E. The Relationship Between Ventilation And Physical Quality Of Houses With Pulmonary Tuberculosis Cases In The Working Area Of Sragen Primary Healthcare Center, Sragen Regency. *J. Kesehat. Lingkung.* **2023**, *15*, 76–83. [CrossRef]
9. Kukuljan, L.; Gabrovšek, F.; Covington, M.D.; Johnston, V.E. CO_2 dynamics and heterogeneity in a cave atmosphere: Role of ventilation patterns and airflow pathways. *Theor. Appl. Climatol.* **2021**, *146*, 91–109. [CrossRef]
10. Class, H.; Keim, L.; Schirmer, L.; Strauch, B.; Wendel, K.; Zimmer, M. Seasonal Dynamics of Gaseous CO_2 Concentrations in a Karst Cave Correspond with Aqueous Concentrations in a Stagnant Water Column. *Geosciences* **2023**, *13*, 51. [CrossRef]
11. Andualem, Z.; Gizaw, Z.; Bogale, L.; Dagne, H. Indoor Bacterial Load and its Correlation to Physical Indoor Air Quality Parameters in Public Primary Schools. *Multidiscip. Respir. Med.* **2019**, *14*, 1–7. [CrossRef] [PubMed]
12. Lario, J.; Soler, V. Microclimate monitoring of Pozalagua cave (Vizcaya, Spain): Application to Management and protection of show caves. *J. Cave Karst Stud.* **2010**, *72*, 169–180. [CrossRef]

13. Tanahara, A.; Taira, H.; Takemura, M. Radon distribution and the ventilation of a limestone cave on Okinawa. *Geochem. J.* **1997**, *31*, 49–56. [CrossRef]
14. Weng, X.; Luo, W.; Wang, Y.; Liu, Y.; Zeng, G.; Lyu, Y.; Chen, J.; Wang, S. Radon-222 in karst caves of Southwestern China: Sources, seasonal dynamics, and human exposure risks. *Ecotoxicol. Environ. Saf.* **2026**, *322*, 120339. [CrossRef] [PubMed]
15. Takahashi, L.C.; Santos, T.d.O.; Pinheiro, R.M.M.; Passos, R.G.; Rocha, Z. Radon Dosimetry Using Solid State Nuclear Track Detectors in Different Environments: A Review. *Appl. Radiat. Isot.* **2022**, *186*, 110217. [CrossRef] [PubMed]
16. Mozzoni, P.; Pinelli, S.; Corradi, M.; Ranzieri, S.; Cavallo, D.; Poli, D. Environmental/Occupational Exposure to Radon and Non-Pulmonary Neoplasm Risk: A Review of Epidemiologic Evidence. *Int. J. Environ. Res. Public Health* **2021**, *18*, 10466. [CrossRef] [PubMed]
17. Nugraha, E.D.; Hosoda, M.; Winarni, I.D.; Prihantoro, A.; Suzuki, T.; Tamakuma, Y.; Akata, N.; Tokonami, S. Dose Assessment of Radium-226 in Drinking Water from Mamuju, a High Background Radiation Area of Indonesia. *Radiat. Environ. Med.* **2020**, *9*, 79–83. [CrossRef] [PubMed]
18. Pradana, R.; Nugraha, E.D.; Omori, Y.; Shilfa, S.N.; Winarni, I.D.; Wahyudi, W.; Untara, U.; Kurnia, I.; Safitri, R.; Kranrod, C.; et al. Public Exposure From Inhalation of Radon and Thoron Around the Tin Mine and Smelter Areas in Bangka, Indonesia. *Sci. Rep.* **2024**, *14*, 30731. [CrossRef] [PubMed]
19. Aswood, M.S.; Alhous, S.F.; Abdulridha, S.A. Life Time Cancer Risk Evaluation Due to Inhalation of Radon Gas in Dwellings of Al-Diwaniyah Governorate, Iraq. *Nat. Environ. Pollut. Technol.* **2022**, *21*, 331–337. [CrossRef]
20. Liu, Y.; Xu, Y.; Xu, W.; He, Z.; Fu, C.; Du, F. Radon and Lung Cancer: Current Status and Future Prospects. *Crit. Rev. Oncol. Hematol.* **2024**, *198*, 104363. [CrossRef] [PubMed]
21. WHO. Radon's Theorem. American Mathematical Society (AMS). Available online: https://www.who.int/news-room/fact-sheets/detail/radon-and-health (accessed on 22 May 2026).
22. Stefanov, P.; Turek, K.; Tsankov, L. Summary Results of Radon-222 Activity Monitoring in Karst Caves in Bulgaria. *Geosciences* **2025**, *15*, 378. [CrossRef]
23. Fijałkowska–lichwa, L.; Tyc, A.; Przylibski, T.A. Radon (^{222}Rn) as a tracer of cave air exchange. *Air Qual. Atmos. Health* **2025**, *18*, 867–897. [CrossRef]
24. Le Roux, R.; Bezuidenhout, J.; Nemangwele, F. Radon concentrations in the Sudwala cave, South Africa. *Arab. J. Geosci.* **2023**, *16*, 250. [CrossRef]
25. Syarbaini, S.; Kusdiana, K.; Wahyudi, W.; Iskandar, D.; Widodo, S.; Dewang, S. Geologic Influence on Radon Concentrations Levels in Cave: A Case Study of Mimpi Cave in the Maros Karst of South Sulawesi, Indonesia. *At. Indones.* **2023**, *49*, 125–130. [CrossRef]
26. Hernández-Gutiérrez, L.E.; Calderón-Guerrero, C.; Martín-Rosales, W.; Rodríguez-Martín, J.; Cruz-Pérez, N.; Hernández-Martín, H.; García-Gil, A.; Santamarta, J.C. Guidelines for Managing Radon Hazards in Tourist Volcanic Caves in Spain. *Geohealth* **2024**, *8*, e2024GH001067. [CrossRef] [PubMed]
27. Panlaqui, A.A.; Ballesteros, F.C.; Dean, K.M.R.; Kranrod, C.; Tokonami, S. Radon and thoron in the ambient air of the caves in Bohol Island, Philippines. *Nucl. Eng. Technol.* **2025**, *57*, 103702. [CrossRef]
28. Chavarria, A.; Golzarri, J.I.; Espinosa, G. Radon Dose Determination and Radiological Risk in Some Mexican Caves with CR-39 Detectors. *J. Nucl. Phys. Mater. Sci. Radiat. Appl.* **2021**, *8*, 169–175. [CrossRef]
29. García Paz, F.A.; Gonzalez Romero, Y.A.; Zalakeviciute, R. Radon (222Rn) concentrations in the touristic Jumandy cave in the Amazon region of Ecuador. *J. Radiat. Res.* **2019**, *60*, 759–767. [CrossRef] [PubMed]
30. Ahmad, N.; Sani, J.M.; Muslim, N.H.; Alias, N.A.; Saat, A. Ventilation effect on the radon-222 annual effective dose inside gua gajah and gua penyu caves, kompleks gua kota gelanggi, Pahang, Malaysia. *Malays. J. Anal. Sci.* **2018**, *22*, 446–451. [CrossRef]
31. Nguyet, N.T.A.; Duong, N.T.; Schimmelmann, A.; Van Huong, N. Human exposure to radon radiation geohazard in Rong Cave, Dong Van Karst Plateau Geopark, Vietnam. *Vietnam J. Earth Sci.* **2018**, *40*, 117–125. [CrossRef]
32. Grant, C.N.; Lalor, G.C.; Balcázar, M. Radon monitoring in sites of economical importance in Jamaica. *Appl. Radiat. Isot.* **2012**, *71*, 96–101. [CrossRef] [PubMed]
33. Alberigi, S.; Pecequilo, B.R.S.; Lobo, H.A.S.; Campos, M.P. Assessment of effective doses from radon levels for tour guides at several galleries of Santana Cave, Southern Brazil, with CR-39 detectors: Preliminary results. *Radiat. Prot. Dosim.* **2011**, *145*, 252–255. [CrossRef] [PubMed]
34. Carrazana González, J.; Ley, O.D.; Åkerblom, G.; León, L.M.; Castillo, R.G. Exposure to radon in tourist caves in Cuba. *Int. J. Low Radiat.* **2010**, *7*, 133–139. [CrossRef]
35. Sajó-Bohus, L.; Greaves, E.D.; Pálfalvi, J.; Urbani, F.; Merlo, G. Radon concentration measurements in Venezuelan caves using SSNTDS. *Radiat. Meas.* **1997**, *28*, 725–728. [CrossRef]
36. UNSCEAR. *Sources and Effects of Ionizing Radiation: UNSCEAR 2024 Report to the General Assembly with Scientific Annexes VOLUME II Scientific Annex B*; United Nations: New York, NY, USA, 2025.

37. Sokić, A.; Perazić, L.; Knežević, I. Measurement of ambient dose equivalent H*(10) in the surrounding of nuclear facilities in Serbia. In *RAD Conference Proceedings*; RAD Association: Darlinghurst, Australia, 2019; pp. 42–46.
38. ICRP. Occupational Intakes of Radionuclides, Part 3. In *Annals of the ICRP 2017*; ICRP: Ottawa, ON, Canada, 2017; Volume 46, pp. 1–487.
39. ICRP. *The 2007 Recommendations of the International Commission on Radiological Protection*; ICRP: Ottawa, ON, Canada, 2007.
40. Government of the Republic of Indonesia. *Ionizing Radiation Safety and Radioactive Material Security*; Government of the Republic of Indonesia: Jakarta, Indonesia, 2023; Volume 45.
41. Samodra, H.; Gafoer, S.; Tjokrosapoetro, S. *Geological Map of the Pacitan Quadrangle, Jawa*; Pusat Penelitian dan Pengembangan Geologi: Bandung, Indonesia, 1992.
42. Fatimah, F. Pemodelan Bawah Permukaan Manifestasi Mineral dengan Metode Geomagnetik Daerah Pacitan Jawa Timur. *KURVATEK* **2019**, *4*, 25–33. [CrossRef]
43. Abuzadan. Seri Peta Kab. Pacitan–Jatim (Bagian 2-Peta Geologi). Available online: https://abuzadan.staff.uns.ac.id/2012/04/13/seri-peta-kab-pacitan-jatim-bagian-2-peta-geologi/ (accessed on 25 October 2026).
44. Natural Earth. Admin 0—Countries. Available online: https://www.naturalearthdata.com/downloads/10m-cultural-vectors/10m-admin-0-countries/ (accessed on 25 October 2026).
45. Pornnumpa, C.; Oyama, Y.; Iwaoka, K.; Hosoda, M.; Tokonami, S. Development of radon and thoron exposure systems at Hirosaki University. *Radiat. Environ. Med.* **2018**, *7*, 13–20. [CrossRef] [PubMed]
46. Saïdou; Tokonami, S.; Hosoda, M.; Simo, A.; Hell, J.V.; German, O.; Meless, E.G.O. From Radon and Thoron Measurements, Inhalation Dose Assessment to National Regulation and Radon Action Plan in Cameroon. *J. Radiat. Prot. Res.* **2022**, *47*, 237–245. [CrossRef]
47. Hu, J.; Yang, G.; Kranrod, C.; Iwaoka, K.; Hosoda, M.; Tokonami, S. An Improved Passive CR-39-Based Direct 222Rn/220Rn Progeny Detector. *Int. J. Environ. Res. Public Health* **2020**, *17*, 8569. [CrossRef] [PubMed]
48. Kranrod, C.; Tamakuma, Y.; Hosoda, M.; Tokonami, S. Importance of discriminative measurement for radon isotopes and its utilization in the environment and lessons learned from using the RADUET monitor. *Int. J. Environ. Res. Public Health* **2020**, *17*, 4141. [CrossRef] [PubMed]
49. Rosianna, I.; Pradana, R.; Nugraha, E.D.; Wahyudi, W.; Farid, M.M.; Permana, S.; Muhammad, A.G.; Muniroh, M.; Amqam, H.; Kranrod, C.; et al. Occupational radiation exposure assessment in tin smelting: An integrated evaluation of external and internal doses from NORM in Indonesia. *Front. Public Health* **2026**, *14*, 1808363. [CrossRef] [PubMed]
50. FTLab Corp. RD201 (Radon Eye Alpha) Product Specifications. Available online: https://radonftlab.com/kr/rd201/ (accessed on 13 August 2026).
51. Bertin Technologies. AlphaE Ultra-Small Radon Monitor. Available online: https://www.bertin-technologies.com/product/radon-professional-monitoring/radon-alphae/ (accessed on 14 November 2026).
52. Liu, C.; Ma, H.; Zeng, Z.; Cheng, J.; Li, J.; Zhang, H. Measurements of Radon Concentrations Using CR-39 Detectors in China JinPing Underground Laboratory (2015–2016). *arXiv* **2018**. [CrossRef]
53. *ISO 16641:2014*; Measurement of Radioactivity in the Environment—Air—Radon 220: Integrated Measurement Methods for the Determination of the Average Activity Concentration Using Passive Solid-State Nuclear Track Detectors. International Organization for Standardization: Geneva, Switzerland, 2014.
54. WHO. *WHO Handbook For Indoor Radon: A Public Health Perspective*; WHO: Geneva, Switzerland, 2009.
55. ICRP. Radiological Protection against Radon Exposure. *Ann. ICRP* **2014**, *43*, 1–328. [CrossRef] [PubMed]
56. IAEA. *Protection of the Public Against Exposure Indoors Due to Radon and Other Natural Sources of Radiation*; IAEA: Vienna, Austria, 2015.
57. Ministry of Employement. *Labour Law of the Republic of Indonesia*; Law No. 13/2003; Ministry of Employement: Jakarta, Indonesia, 2003.
58. Salazar-Carballo, P.A.; López-Pérez, M.; Martín-González, M.E.; Hernández-Suarez, F.; Martín-Luis, M.C. Radon Dynamics and Effective Dose Estimation in a Touristic Volcanic Cave: La Cueva del Viento, Tenerife (Canary Islands, Spain). *Geohealth* **2023**, *7*, e2022GH000704. [CrossRef] [PubMed]
59. Fontenot, J.D.; Taddei, P.; Zheng, Y.; Mirkovic, D.; Newhauser, W.D. Ambient dose equivalent versus effective dose for quantifying stray radiation exposures to a patient receiving proton therapy for prostate cancer. *Nucl. Technol.* **2009**, *168*, 173–177. [CrossRef] [PubMed]
60. Lüttke, T.; Kunze, C.; Flesch, K.; Dilling, J.; Fohlmeister, J.; Hummrich, H.; Arndt, R.; Krzikalla, A.; Lucks, C.; Kuhn, T. Estimations of effective doses received from naturally occurring radioactivity in polymetallic nodules from the deep sea. *Sci. Rep.* **2025**, *15*, 32303. [CrossRef] [PubMed]
61. IAEA. Protection of Workers Against Exposure Due to Radon. 2024. Available online: www.iaea.org (accessed on 6 August 2026).

62. Sánchez-Moral, S.; Lario, J.; Cuezva, S.; Cañaveras, J.C.; Martín-Pozas, T.; Fernández-Cortés, A. Protocol for assessing and managing radon gas exposure risks in caves: A case study of Altamira and Paleolithic cave art of Northern Spain World Heritage Site. *Int. J. Speleol.* **2025**, *54*, 5. [CrossRef]
63. Šebela, S.; Novak, U.; Kogovšek, B. Air Pressure Perturbations in Karst Caves and Waters after the Hunga Tonga–Hunga Ha'apai Volcano Eruption on 15 January 2022. *Atmosphere* **2023**, *14*, 1088. [CrossRef]
64. Nugraha, E.D.; Hosoda, M.; Kusdiana; Untara; Mellawati, J.; Nurokhim; Tamakuma, Y.; Ikram, A.; Syaifudin, M.; Yamada, R.; et al. Comprehensive exposure assessments from the viewpoint of health in a unique high natural background radiation area, Mamuju, Indonesia. *Sci. Rep.* **2021**, *11*, 14578. [CrossRef] [PubMed]
65. Hassan, N.M.; Hosoda, M.; Ishikawa, T.; Sorimachi, A.; Sahoo, S.K.; Tokonami, S.; Fukushi, M. Radon Migration Process and Its Influence Factors; Review. *J. Health Phys.* **2009**, *44*, 218–231. [CrossRef]
66. Gregorič, A.; Vaupotič, J.; Šebela, S. The role of cave ventilation in governing cave air temperature and radon levels (Postojna Cave, Slovenia). *Int. J. Climatol.* **2014**, *34*, 1488–1500. [CrossRef]
67. Schumann, R.; Gundersen, L.; Tanner, A. Geology and occurrence of radon. In *Radon: Prevalence, Measurements, Health Risks and Control*; American Society for Testing and Materials: West Conshohocken, PA, USA, 1994; pp. 83–96.
68. Ma, P.; Sun, Q.; Geng, J.; Hu, J.; Xue, L.; Wen, N.; Lyu, C.; Wang, W.; Jie, S.; Wang, Z. Radon exhalation and migration mechanisms across stratigraphic units: A case study from Inner Mongolia. *J. Environ. Radioact.* **2026**, *294*, 107934. [CrossRef] [PubMed]
69. Rowberry, M.D.; Martí, X.; Frontera, C.; Van De Wiel, M.J.; Briestenský, M. Calculating flux to predict future cave radon concentrations. *J. Environ. Radioact.* **2016**, *157*, 16–26. [CrossRef] [PubMed]
70. Buzjak, N.; Gabrovšek, F.; Perșoiu, A.; Pennos, C.; Paar, D.; Bočić, N. CO_2 Emission from Caves by Temperature-Driven Air Circulation—Insights from Samograd Cave, Croatia. *Climate* **2024**, *12*, 199. [CrossRef]
71. Waring, C.L.; Hankin, S.I.; Solomon, S.B.; Long, S.; Yule, A.; Blackley, R.; Werczynski, S.; Baker, A. Cave radon exposure, dose, dynamics and mitigation. *J. Cave Karst Stud.* **2021**, *83*, 1–19. [CrossRef]
72. Liu, Z.; Liu, W.; Liu, H.; Gao, T.-P.; Zhao, H.-X.; Li, G.; Han, H.-F.; Li, Z.-J.; Lal, R.; Ning, T.-Y. Capture of soil respiration for higher photosynthesis with lower CO_2 emission. *J. Clean. Prod.* **2020**, *246*, 119029. [CrossRef]
73. Alvarez-Gallego, M.; Garcia-Anton, E.; Fernandez-Cortes, A.; Cuezva, S.; Sanchez-Moral, S. High radon levels in subterranean environments: Monitoring and technical criteria to ensure human safety (case of Castañar cave, Spain). *J. Environ. Radioact.* **2015**, *145*, 19–29. [CrossRef] [PubMed]
74. Smetanová, I.; Haviarová, D.; Pristašová, L.; Csicsay, K. Radon concentration and effective dose assessment in the Brestovská Cave and the Demänovská Cave of Liberty, Slovakia. *Eur. Phys. J. Spec. Top.* **2026**, *235*, 9815–9826. [CrossRef]
75. Tokonami, S. Characteristics of Thoron (220Rn) and Its Progeny in the Indoor Environment. *Int. J. Environ. Res. Public Health* **2020**, *17*, 8769. [CrossRef] [PubMed]
76. Hwa Oh, Y.; Kim, G. A radon-thoron isotope pair as a reliable earthquake precursor. *Sci. Rep.* **2015**, *5*, 13084. [CrossRef] [PubMed]
77. Smith, A.C.; Wynn, P.M.; Barker, P.A. Natural and anthropogenic factors which influence aerosol distribution in Ingleborough Show Cave, UK. *Int. J. Speleol.* **2013**, *42*, 49–56. [CrossRef]
78. Dredge, J.; Fairchild, I.J.; Harrison, R.M.; Fernandez-Cortes, A.; Sanchez-Moral, S.; Jurado, V.; Gunn, J.; Smith, A.; Spötl, C.; Mattey, D.; et al. Cave aerosols: Distribution and contribution to speleothem geochemistry. *Quat. Sci. Rev.* **2013**, *63*, 23–41. [CrossRef]
79. Sultani, M.A.; Bulko, M.; Müllerová, M.; Masarik, J.; Eckertová, T.I. Interaction between radon progeny and particulate matter in an urban environment. *J. Environ. Radioact.* **2026**, *294*, 107918. [CrossRef] [PubMed]
80. Chen, J.; Harley, N.H. A Review of Radon Equilibrium Factors in Underground Mines, Caves, and Thermal Spas. *Health Phys.* **2020**, *119*, 342–350. [CrossRef] [PubMed]
81. Prasad, M.; Rawat, M.; Dangwal, A.; Kandari, T.; Gusain, G.; Mishra, R.; Ramola, R. Variability of radon and thoron equilibrium factors in indoor environment of Garhwal Himalaya. *J. Environ. Radioact.* **2016**, *151*, 238–243. [CrossRef] [PubMed]
82. Grygier, A.; Skubacz, K. Radon Equilibrium Factor and the Assessment of the Annual Effective Dose at Underground Workplaces. *Atmosphere* **2024**, *15*, 1131. [CrossRef]
83. Aldrian, E.; Dwi Susanto, R. Identification of three dominant rainfall regions within Indonesia and their relationship to sea surface temperature. *Int. J. Climatol.* **2003**, *23*, 1435–1452. [CrossRef]
84. The Meteorology C and GA. Tropical Climate. Available online: https://gaw-bariri.bmkg.go.id/publikasi/gawsarium/249-iklim-tropis (accessed on 14 November 2026).
85. Statistics of Pacitan Regency. *Pacitan Regency in Figures: 2026*; Statistics of Pacitan Regency: Pacitan, Indonesia, 2026.
86. Przylibski, T.A. Radon concentration changes in the air of two caves in Poland. *J. Environ. Radioact.* **1999**, *45*, 81–94. [CrossRef]
87. Syarbaini, S.A. Terrestrial gamma radiation exposure in Bangka-Belitung Islands, Indonesia. *At. Indones.* **2015**, *41*, 41–45. [CrossRef]
88. Markovic, V.M.; Krstic, D.; Nikezic, D.; Stevanovic, N. Doses from radon progeny as a source of external beta and gamma radiation. *Radiat. Environ. Biophys.* **2012**, *51*, 391–397. [CrossRef] [PubMed]

89. Kessler, P.; Camp, A.; Dombrowski, H.; Neumaier, S.; Röttger, A.; Vargas, A. Influence Of Radon Progeny On Dose Rate Measurements Studied At Ptb's Radon Reference Chamber. *Radiat. Prot. Dosim.* **2017**, *177*, 407–414. [CrossRef] [PubMed]
90. Nugraha, E.D.; Modibo, O.B.; Pradana, R.; Merdekawati, R.; Megagasri, K.; Topandi, A.; Rachman, A.; Kurniawan, R.; Fajrianshah, E.; Hidayati, N. Radon exhalation rate and natural radioactivity in the building materials used in metropolitan Jakarta and its surrounding areas, Indonesia. *Front. Public Health* **2025**, *13*, 1539957. [CrossRef] [PubMed]
91. Anderson, J.L.; Zwack, L.M.; Brueck, S.E. Exposure to Radon and Progeny in a Tourist Cavern. *Health Phys.* **2021**, *120*, 628–634. [CrossRef] [PubMed]
92. Maier, A.; Bailey, T.; Hinrichs, A.; Lerchl, S.; Newman, R.T.; Fournier, C.; Vandevoorde, C. Experimental Setups for In Vitro Studies on Radon Exposure in Mammalian Cells—A Critical Overview. *Int. J. Environ. Res. Public Health* **2023**, *20*, 5670. [CrossRef] [PubMed]
93. Kashkinbayev, Y.; Kazhiyakhmetova, B.; Altaeva, N.; Bakhtin, M.; Tarlykov, P.; Saifulina, E.; Aumalikova, M.; Ibrayeva, D.; Bolatov, A. Radon Exposure and Cancer Risk: Assessing Genetic and Protein Markers in Affected Populations. *Biology* **2025**, *14*, 506. [CrossRef] [PubMed]
94. Harrison, J.D.; Balonov, M.; Bochud, F.; Martin, C.; Menzel, H.-G.; Ortiz-Lopez, P.; Smith-Bindman, R.; Simmonds, J.; Wakeford, R. ICRP Publication 147: Use of Dose Quantities in Radiological Protection. *Ann. ICRP* **2021**, *50*, 9–82. [CrossRef] [PubMed]

Disclaimer/Publisher's Note: The statements, opinions and data contained in all publications are solely those of the individual author(s) and contributor(s) and not of MDPI and/or the editor(s). MDPI and/or the editor(s) disclaim responsibility for any injury to people or property resulting from any ideas, methods, instructions or products referred to in the content.